Two phase modelling of Geldart B particles in a novel indirectly heated bubbling fluidized bed biomass steam reformer

Tsekos, C.; de Voogt, D.; de Jong, W.; Padding, J. T.

Important note
To cite this publication, please use the final published version (if applicable).
Please check the document version above.

Two phase modelling of Geldart B particles in a novel indirectly heated bubbling fluidized bed biomass steam reformer

C. Tsekos [*], D. de Voogt, W. de Jong, J.T. Padding

Faculty of Mechanical, Maritime and Materials Engineering, Process and Energy Department, Delft University of Technology, Leeghwaterstraat 39, Delft 2628 CB, Netherlands

ARTICLE INFO

ABSTRACT

This work focuses on the numerical modelling and experimental validation of the hydrodynamic behaviour of a novel 50 kW$_{th}$ indirectly heated bubbling fluidized bed steam reformer. The hydrodynamic behaviour of fluidized beds with immersed vertical tubes and complex fluidized bed geometries in general have not been thoroughly investigated in terms of numerical modelling coupled with experimental validation for pilot scale reactors. Therefore, the present study contributes to the fluidized bed hydrodynamics numerical modelling field, while investigating a novel reactor concept. Simulations were performed employing the Two-Fluid Model approach, using the Kinetic Theory of Granular Flows (KTGF) and the adjusted Syamlal O'Brien drag model. The reactor's hydrodynamic behaviour was simulated successfully, as showcased by a comparison of global hydrodynamic metrics (bed height, pressure drop) between computational and experimental results. Simulations were performed with and without considering an additional nitrogen gas feed on the side of the reactor (feeding system pressurization). Overall, for both cases, for realistic values of the particle restitution coefficient channelling of the gas flow near the reactor walls was observed. Larger bubbles appeared to be forming near the outer wall of the reactor for the no side-flow simulations. The opposite behaviour was encountered for the side-flow simulations due to stream-like behaviour of the side-flow moving up against the reactor's outer wall. The choice to limit the simulations to a 72° symmetry domain was validated, indicating the possibility of further reduction. Finally, it was argued that increasing the reactor's diameter could potentially lead to a reduction of the observed channelling of the fluidization media and improve the mixing achieved in the reactor and thus the conversion efficiency of the IHBFBSR during gasification applications.

1. Introduction

The growing concern for environmental change, the depletion of fossil fuel reserves, as well as the increasing need for energy self-reliance, have led to the employment of sustainable resources for heat and power generation as well as for fuels and chemicals production. Biomass materials constitute the third most abundant fuel resource, following coal and oil, and provide a potentially clean and renewable alternative fuel, also readily available worldwide. Thermochemical processes such as pyrolysis, torrefaction, gasification and hydrothermal liquefaction, constitute interesting options for the conversion of biomass fuels to useful products [1]. Gasification in particular, can be defined as the thermochemical conversion process through which carbonaceous materials are converted to a fuel gas or chemical feedstock in an oxygen deficient (reducing) environment, while requiring heat [2].

Gasifiers can be classified according to various of their characteristics. One type of classification is according to the gas–solid interaction within the reactor, which includes fixed or moving bed (downdraft, updraft, crossdraft) gasifiers, fluidized bed gasifiers (bubbling, circulating and dual) and entrained flow gasifiers (top-fed and side-fed). The gasification medium employed in the process (air, CO_2, steam, etc.) provides another classification parameter [2,3]. The way that the heat required for the gasification of a feedstock is provided to the system constitutes another differentiating factor between gasification systems. When the feedstock is partially oxidized by the gasification agent (usually air or O_2), the process is referred to as autothermal or direct gasification. In this case, the heat required for the fuel heating, drying, pyrolysis and gasification reactions is provided by exothermal oxidation reactions occurring within the gasifier. When an oxidising agent is absent, an external energy source is required and the process is then called

allothermal or indirect gasification, with steam being most commonly employed as an allothermal gasification agent [4,5]. The biggest limitation of autothermal gasification is the requirement of separation/removal of diluent gases such as N_2, either downstream (from the syngas) or upstream (from air) the gasification unit [6]. Thus, allothermal gasification technologies constitute an attractive option.

Heat required for the operation of allothermal gasifiers can be provided through discontinuous intermittent operation of a single fluidized bed, through the circulation of particles between two interconnected fluidized beds, or finally by employing heat transfer surfaces [7]. The first category includes mainly Winkler's fluidized bed gasifier (1922) where air (or later O_2) blown combustion up to 1100–1200 °C was employed, repeatedly followed by steam gasification. In recent years the focus of the scientific community has been mostly on the other two technologies. The interconnected fluidized beds gasification technology, or Dual Fluidized Bed (DFB) gasification, utilizes two separate gasification and combustion reactors [8,9]. A thorough literature review and technical analysis of the DFB gasification technology can be found in [7] and even more recent ones in [10] and [11]. In heat exchanger configurations, one concept completely separates the gasification area from the "heat provision reactor" in order to allow the application of a variety of fuels and/or processes. Juentgen and van Heek suggested such a concept in 1975 [12], incorporating helium produced from nuclear reactors at high temperatures (HTR), which was however abandoned due to the poor heat transfer [13]. Another concept was the MTCI gasifier, where a pulse combustor fed the heat exchanger tubes located in the main steam blown atmospheric fluidized bed reactor, using the gasification product gas. Turbulent flue gas flow and low frequency acoustic oscillations from pulse combustion can lead to improved heat transfer compared to conventional heat exchangers [7,14]. The most recent concept in this category is the Biomass Heatpipe Reformer. In this case gasification takes place in a pressurized chamber and the required heat is generated in a combustion chamber below it and exchanged through a number of heat pipes. Both the gasifier and the combustor are fluidized bed reactors, while for the heat pipes the working fluid (Na, K, etc.) evaporates on the combustor side and condenses on the gasifier one [15–17]. The use of this particular concept is claimed to increase heat transfer coefficients and reduce the required heat transfer areas 10 to 20 times [13].

In general, gas–solid fluidized beds are widely used in process industries and biomass gasification in particular, due to their ability to combine reactor and mixer capabilities and facilitate continuous operation [18]. Compared to other gas–solid reactor types, fluidized bed gasifiers offer significant advantages, such as rapid mixing and consequently almost isothermal conditions, high heat and mass transfer rates between gas and particles also leading to smaller required surface area of heat exchangers within the bed, suitability for large-scale operations and more [19]. Due to their importance for the process industry, fluidized beds have been widely studied, in order to better describe fluidization phenomena both experimentally and computationally. However, in particular the lack of understanding of dense gas-particle flow fundamentals creates difficulties in designing and scaling-up such systems. Therefore, designing a fluidized bed reactor often becomes an empirical process, requiring expensive and time consuming preliminary pilot-scale experiments [20]. This task becomes even more challenging when non-standard or complex reactor geometries are employed. Therefore the development of numerical models for the simulation of fluidized beds hydrodynamics with such geometries is of the outmost importance for the corresponding scientific community.

Complex fluidized bed geometries have been thoroughly studied in the literature in terms of numerical models development, however almost solely in the form of horizontally immersed tubes in a fluidized bed reactor. Most commonly, Eulerian – Lagrangian methods have been employed in their study. The CFD-DEM (Computational Fluid Dynamics-Discrete Element Method) has been widely applied [21–25], also coupled with various methods, such as the coarse grain (CG) model [26],

the immersed boundary method (IBM) [27–29], the virtual dual-grid model (VDGM) [30,31], the cut cell technique in a MFIX (Multiphase Flow with Interphase Exchange) solver [32,33], the fictitious domain (FD) method [34,35], LES (large eddy simulation) [36,37], as well as with a combination of the signed distancing function (SDF) with the IMB and CG models [38]. Hard sphere, CFD-DPM (Computational Fluid Dynamics-Discrete Particle Method) models have also been employed for the simulation of complex geometries [39,40]. Furthermore, Córcoles et al. [41] presented the simulation of a bubbling fluidized bed with immersed surfaces, using a Computational Particle Fluid Dynamics (CPFD) model, based on the multiphase particle-in-cell (MP − PIC) method. Eulerian – Eulerian two-fluid models (TFM) have also been employed for the simulation of similar geometries, however to a lesser extent [42–50]. In a conceptually different approach then for the cases described above, Jašo et al. [51], investigated a fluidized bed membrane reactor for oxidative methane coupling via CFD simulations. In an effort to investigate the effect of distributed oxygen feed on the reactor performance several symmetrically arranged vertical tubes were placed in a cylindrical reactor geometry. A Eulerian–Eulerian granular kinetic flow model was used for the simulation of the fluidized bed, coupled with reaction kinetics, while a lab scale reactor with a diameter of 40 mm was used for experimental validation. The analysis of the results showed that certain vertical tube configurations influence hydrodynamics in such a way that the bottom-fed gas preferably follows a path near the walls of the reactor. A similar reactor concept was simulated by de Jong et al. [52], employing a hybrid DPM-IBM method, however without experimental validation. From their findings it became apparent that horizontal membrane tubes lead to reduced bubble size compared to vertical ones. Finally, Verma et al. [53] employed a TFM coupled with the cut-cell method in MFIX, to investigate the hydrodynamics of 3D fluidized beds containing vertical U-tubes banks, inspired from the design of carbon capture units. According to the authors, the presence of the vertical tubes leads to decreased bubble diameter, while their presence divides the bed into smaller, parallel gas–solid flow chambers.

The focus of this work lies on the numerical modelling and experimental validation, of the hydrodynamic behaviour of a novel 50 kW$_{th}$ indirectly heated bubbling fluidized bed steam reformer (IHBFBSR). This pilot-scale reactor was designed, built and commissioned by the Dutch company Petrogas - Gas Systems together with the Process and Energy Department of Delft University of Technology. In this novel reactor concept two radiant tube natural gas burners, one in the bottom (bed area) and one in the top (freeboard) of the reactor, provide the heat necessary for gasification (Fig. 1). Its design aims at the reduction of heat losses, the provision of enough heat for the realization of the biomass steam reforming and cracking reactions and the exploration of scale-up possibilities to an industrial scale process. The IHBFBSR concept proposes a novel approach on indirect gasification technology, with its unique reactor design. More details regarding this novel reactor's positioning among similar technologies as well as the results of its commissioning gasification experiments can be found in [54]. Overall, studying this complex geometry by employing a more narrow cylindrical fluidized bed of equivalent hydrodynamic radius would constitute an oversimplification which would lead to the loss of information and not allow the representation of flow patterns critical to both the present operation and the scale-up of this novel reactor. As it became apparent from the previous discussion, the hydrodynamic behaviour of fluidized beds with immersed vertical tubes has not been thoroughly reported in literature. Furthermore, complex fluidized bed geometries in general have not been thoroughly investigated in terms of numerical modelling coupled with experimental validation for pilot scale reactors. Therefore, it can be argued that the present study, apart from investigating a novel reactor concept, adds also to the field of fluidized bed hydrodynamics numerical modelling. According to the knowledge of the authors, the combination of CFD simulations and experiments on the hydrodynamics of a pilot scale bubbling fluidized bed with an immersed vertical tube (complex geometry) has not been previously reported in the literature.
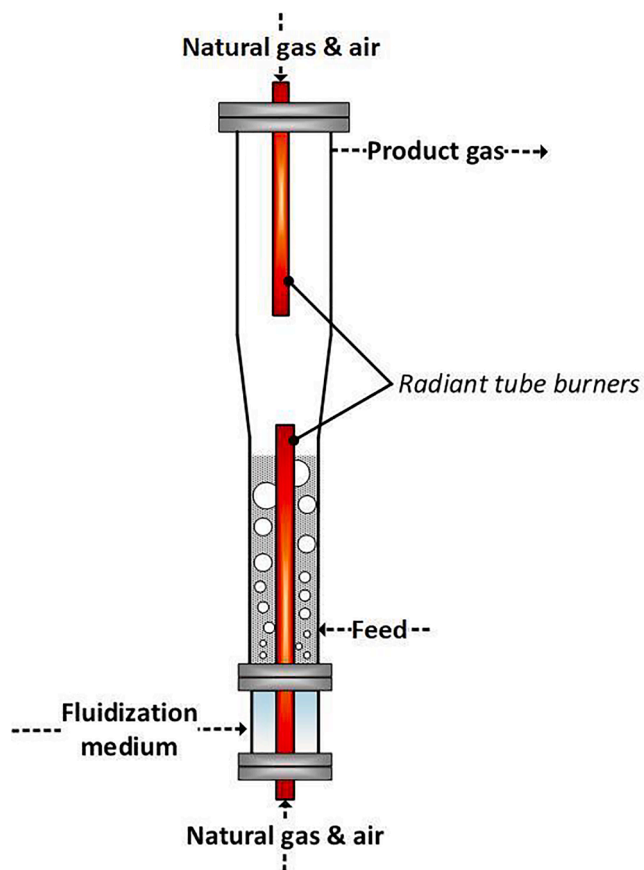
Fig. 1. Conceptual design of the indirectly heated bubbling fluidized bed steam reformer (IHBFBSR).

The numerical simulation of the fluidized bed's hydrodynamic behaviour was performed employing the Eulerian – Eulerian TFM approach. This choice was made with the large scale of the modelled fluidized bed in mind, due to the relatively lower computational costs of TFM versus DPM [55]. Conventional Eulerian-Langragian methods (DPM or DEM) which track individual particles, or even CG models which track particle "clusters" which are in general more favourable for large-scale systems modelling [56], would require the tracking of approximately 10^8 particles given the scale of the setup, even in a reduced simulation domain. Finally, it should be mentioned that in the context of this work the TFM model was used as a tool for studying the hydrodynamic behaviour of the IHBFBSR. Focusing on TFM method development was outside the scope of the present work.

2. Experimental setup

2.1. Reactor description

In the 50 kW$_{th}$ IHBFBSR, biomass gasification experiments with air, nitrogen, steam or combinations of the above as fluidization media can be performed. However, for the hydrodynamic study performed within this work only air and N$_2$ were employed. A detailed presentation of steam/air gasification experiments in the IHBFBSR can be found in [54]. The reactor was manufactured out of 310S (AISI) steel with a wall thickness of 4.78 mm and a height of ~ 3 m. It is insulated with a 200 mm three layer mattress material. The dimensions of the reactor, along with the location of instrumentation equipment (thermocouples and pressure gauges) are presented in Fig. 2. Data from the various instruments were recorded through a SCADA/PLC coupling employing a LabVIEW interface, every 10 s.

Before the test, 75 kg of bed material was inserted in the bed area of

the IHBFBSR. The bed material employed was corundum, an aluminium oxide (Al$_2$O$_3$) containing also traces of iron oxide, titanium oxide and silica. This material, supplied by Unicorn ICS B.V., has a density of 3940 kg/m^3, a hardness of 9 Mohs and its melting point is 1950 °C. The mean particle diameter of the bed material was 543 μm, which classifies it in the Geldart B category (sand-like) of solids in bubbling fluidized beds [57]. The particle size distribution of the corundum bed material was determined using a Microtrac FLEX 10.6.2. Corundum has a very high hardness, thus the probability of fines production due to attrition of the particles is reduced. Furthermore, depending on the fluidization conditions, it has very good heat distribution properties [58].

Two self-recuperative ceramic burners supplied by WS – Wärmeprozesstechnik GmbH were used for the provision of heat in the IHBFBSR. Both were placed inside metal radiant tubes for protection from bed material blasting. Both burners operate in an on/off mode, with the bottom burner being controlled by the average values of thermocouples TC01 – TC05 and the top burner by TC07. The set point of the two burners in the context of the present work was 640 °C, which was the maximum achievable temperature without the employment of in-bed combustion. The burners operate at a constant capacity of 20 kW$_{th}$ and 12 kW$_{th}$ for the bottom (REKUMAT C100) and top one (REKUMAT C80), respectively. The total main body length of the bottom radiant tube is ~ 1.7 m, and 1.2 m of this is situated in the bed area. The bottom part of the radiant tube also warmed up the windbox, as shown in Fig. 2. The top radiant tube is smaller, both in terms of diameter (0.1 m) and of total main body length (1.3 m).

The fluidization media employed in the present study (air and N$_2$) were introduced in the reactor through a distributor plate, after passing through a 6 kW preheater. Depending on the total amount of gases introduced, their inlet temperature ranged between 515 and 620 °C. The distributor plate consisted of 50 tuyeres, each with 2 mm holes drilled in a 20° downwards angle. Nitrogen was also employed to pressurize the feeding system and to prevent obstruction of the pressure gauge in the reactor. For the latter, for each pressure gauge, a 5 ml/min N$_2$ flow was introduced, while approximately 4 kg/h of N$_2$ was introduced in the reactor through the feeding system for the aforementioned purpose. The biomass feeder outlet in the reactor was located 170 mm above the distributor plate and its inside diameter was 50 mm. As can be observed in Fig. 2, pressure gauges located in four spots within the reactor, along with their respective pressure transmitters, were used to record the pressure drops over the distributor plate, the bed zone and the freeboard.

2.2. Hydrodynamics experiments

The main purpose of the experiment presented in this section, was to determine the fluidization characteristics of the IHBFBSR. Since visual observation is not possible in the IHBFBSR, the variation of the bed height during an experiment can be deduced from the thermocouple readings. An example is shown in Fig. 3, where fluidization apparently occurs after roughly 58 min. After this point, the reading of TC01, TC02 and TC03 begin to coincide, with the last one joining this group approximately 10 min later. From this behaviour, it can be safely deduced that the top of the particle bed is located between TC03 and TC04. Air and N$_2$ were introduced through the distributor plate at 22 and 26 kg/h, respectively, and the total mass flow remained unchanged until the temperature set point (640 °C average temperature) was achieved and the system was stabilized (234 min). The secondary N$_2$ side-flow through the feeder was stable at 4.11 kg/h during the experiment. After the previously mentioned point, the fluidization media flow was gradually reduced in steps of 1 kg/h. The first bed height reduction (1st BHR) point was observed when the total flow was firstly reduced to 22 and 25 kg/h of air and N$_2$, respectively. Subsequent to reducing the flow of N$_2$, the temperature recorded by TC03 started to increase compared to TC01 and TC02. This observation suggests that TC03, no longer "insulated" by the fluidized bed material, experiences the heat
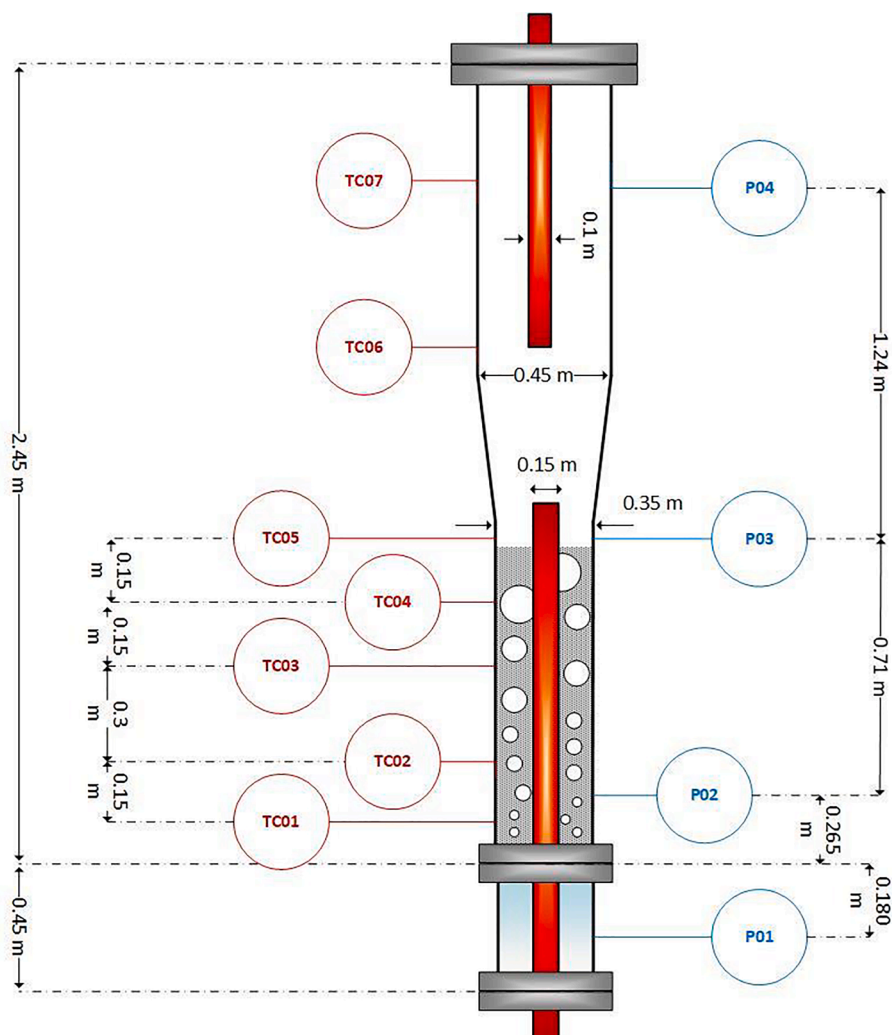
Fig. 2. Basic dimensions of IHBFBSR and instrumentation (thermocouples – TC and pressure gauges – P locations).

produced by the burner unobstructed. By continuing the reduction of the gas flows, such an observation will however no longer be possible. This is because the de-fluidized bed height is 0.591 m and thus located above the location of TC02. Consequently, the only other variation that can be observed is the de-fluidization of the bed, in the 2nd bed height reduction point. At this point, which was achieved for 14 kg/h of air only, the temperatures of TC01 and TC02 started to diverge. Additionally, the de-fluidization was also observed from Fig. 3, where for 14 kg/h of air only, the pressure difference dipped dramatically. In order to ensure that this was indeed the flow rate corresponding to the minimum fluidization velocity (u_{mf}), the flow was gradually zeroed. Finally, in the subsequent gradual increase of the air flow, fluidization was reinstated at 15 kg/h, which was observed both by the thermocouple and the pressured drop readings.

From the aforementioned analysis of the experiment conducted in the IHBFBSR, the data included in Table 1 was used as input for the model developed within this work. The packing limit was estimated as the ratio of the bulk density and the actual density of corundum (1636/3950 = 0.414) and therefore the void fraction at minimum fluidization conditions was calculated ($\alpha_{mf} = 1 - 0.414 = 0.586$). Subsequently, the void fraction (α) at the 1st BHR point was estimated by the following formula [19]:.

$$\frac{H_{mf}}{H} = \frac{(1-\alpha)}{(1-\alpha_{mf})}$$

where H_{mf} is the minimum fluidization bed height and α_{mf} the void fraction at minimum fluidization conditions. For the numerical model developed within this work and which will be presented in the following section, the 53 min of steady state before the 1st BHR point were used for validation. The data obtained regarding the minimum fluidization conditions were used as inputs for the Adjusted Syamlal model. The temperature throughout the bed area for the validation BHR point, as measured by TC01, TC02 and TC03, was assumed to be at a constant value of 600 °C. The temperature of the main gases (air, N_2) and the side-flow (N_2) entering the reactor was also assumed to be 600 °C. As mentioned in Section 2.1, this is very close to the actual value for the main gases. For the side-flow, its small amount relative to the reactor's size, permits this simplification. The average pressure drop over the bed at this point was 55 mbar, while the corresponding bed height was between 0.67 m (TC03) and 0.82 m (TC04). The reason for choosing this interval for the validation, was that after the 1st BHR point the bed area enters a transient state due to a variation in the flow rate. The time spent at each subsequent set point (~3 min) did not suffice for a steady state to be re-established. It should also be mentioned that given the location of P02, which is not at zero height with respect to the distributor plate, the pressure drop between P02 and P03 does not correspond to the pressure drop across the entirety of the bed material, but rather approximately 60 % of the overall bed mass. This will be taken into account in the model validation.
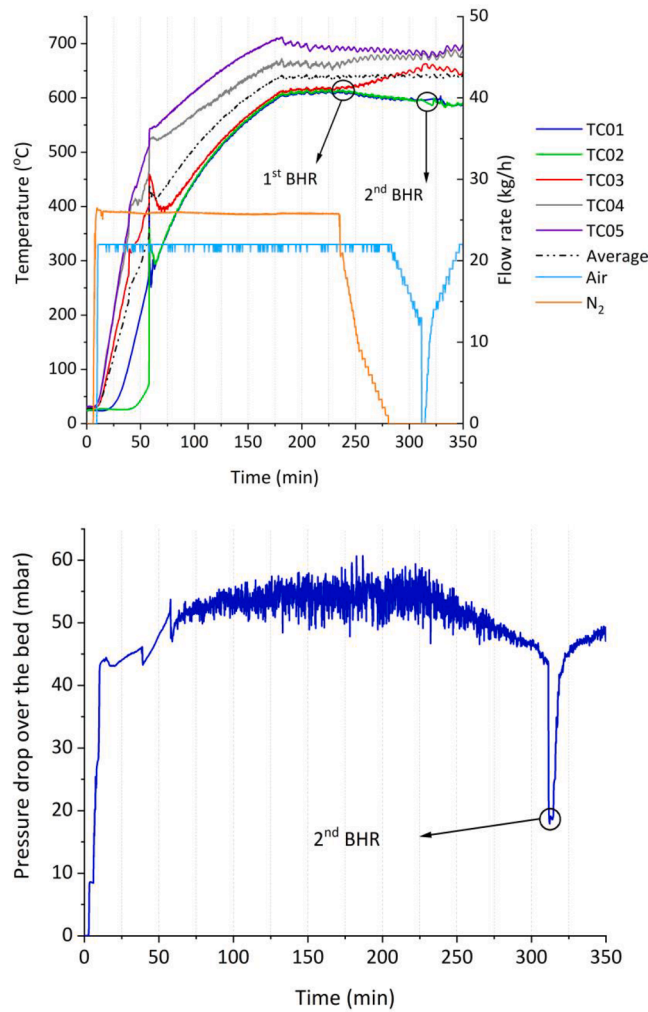
Fig. 3. Top: Air and N_2 flow rates and temperature profile of the IHBFBSR bed zone (TC01-TC05) with the bed height reduction (BHR) points marked during the fluidization experiment conducted in the IHBFBSR. Bottom: Pressure drop over the bed during the fluidization experiment conducted in the IHBFBSR.

3. Numerical model

In the two-fluid continuum model (TFM), both gas and solid phases are described as fully interpenetrating continua using a generalized form of the Navier-Stokes equations. The accumulation of mass in each phase is balanced by the convective mass fluxes, while the sum of all fractions in a cell is equal to unity. The non-steady continuity equations for the gas (g) and solid (s) phases are given below [59],.

$$\frac{\partial}{\partial t}\left(a_g\rho_g\right) + \nabla\bullet\left(a_g\rho_g\overrightarrow{u_g}\right) = 0 \quad \frac{\partial}{\partial t}\left(a_s\rho_s\right) + \nabla\bullet\left(a_s\rho_s\overrightarrow{u_s}\right) = 0 \quad (1)$$

where α is the volume fraction, ρ is the density and u is the velocity of the corresponding phase. According to Newton's second law of motion, momentum change equals to the sum of forces in a domain. The momentum equations for the gas and the solid phase are:

$$\frac{\partial}{\partial t}\left(a_g\rho_g\overrightarrow{u_g}\right) + \nabla\bullet\left(a_g\rho_g\overrightarrow{u_g}\overrightarrow{u_g}\right) = -a_g\nabla p_g - \nabla\bullet\overline{\tau_g} + a_g\rho_g\overrightarrow{g} + K_{gs}\left(\overrightarrow{u_s} - \overrightarrow{u_g}\right) \quad \frac{\partial}{\partial t}\left(a_s\rho_s\overrightarrow{u_s}\right) + \nabla\bullet\left(a_s\rho_s\overrightarrow{u_s}\overrightarrow{u_s}\right) = -a_s\nabla p_s - \nabla p_s - \nabla\bullet\overline{\tau_s} + a_s\rho_s\overrightarrow{g} + K_{gs}\left(\overrightarrow{u_g} - \overrightarrow{u_s}\right) \quad (2)$$

where $\overline{\tau}$ is the stress tensor and p is the pressure of the corresponding phase, and K_{gs} is the interphase exchange coefficient. To account for the particle–particle interactions, the kinetic theory of granular flow (KTGF)

Table 1
Fluidization data obtained from the corresponding experiment in the IHBFBSR.

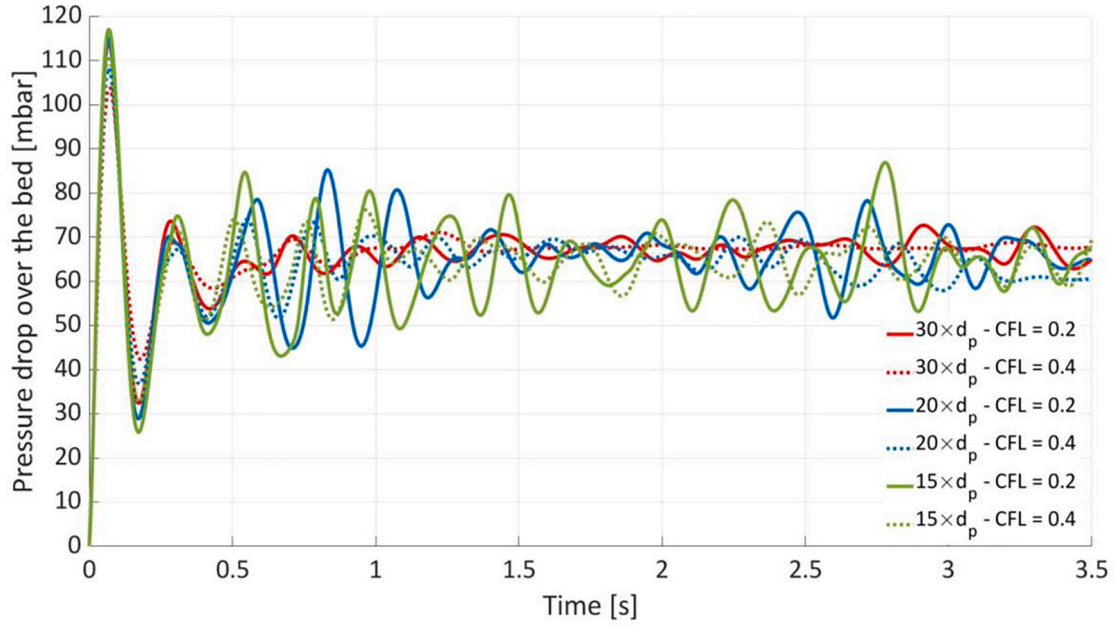|	Air	N_2	Secondary N_2	Total volumetric flow rate	Height	Void fraction
	(kg/h)	*(kg/h)*	*(kg/h)*	*(m^3/h)*	*(m)*	*(-)*
1st BHR	22	26	4	136	0.67	0.63
2nd BHR	14	0	4	52	0.59	0.59

Fig. 4. Pressure drop over the bed area for different grid size and CFL combinations from the IHBBFBSR hydrodynamics simulations without a side-flow.

was employed to predict the solid's fluctuation energy. The granular temperature Θ_s, which represents the energy associated with the particles' fluctuating velocity is given by the following formula [60]:

$$\frac{3}{2}\left[\frac{\partial}{\partial t}(\rho_s a_s \Theta_s) + \nabla\bullet(\rho_s a_s \overrightarrow{u_s}\Theta_s)\right] = -\left(p_s \overrightarrow{I} + \overline{\tau_s}\right)$$
$$: \nabla\overrightarrow{u_s} + \nabla\bullet(k_{\Theta_s}\nabla\Theta_s) - \gamma + \varphi_{gs} \quad (3)$$

The collisional dissipation of energy fluctuations γ represents the energy loss due to particle collisions and is derived from [61]:

$$\gamma = \frac{12(1-e^2)g_0}{d_s\sqrt{\pi}}\rho_s a_s^2 \Theta_s^{\frac{3}{2}} \quad (4)$$

In the above formula, g_0 is the radial distribution coefficient at contact and e is the restitution coefficient. The radial distribution coefficient at contact describes the increased probability of collisions between particles, caused by structure formation in dense suspensions of particles, and is given by [62]:

$$g_0 = \left[1 - \left(\frac{a_s}{a_{s_{max}}}\right)^{\frac{1}{3}}\right]^{-1} \quad (5)$$

The diffusion coefficient for granular temperature k_{Θ_s} was calculated using the Syamlal-O'Brien formulation [63]:

$$k_{\Theta_s} = \frac{15d_s\rho\sqrt{\Theta_s\pi}}{4(41-33\eta)}\left[1 + \frac{12}{5}\eta^2(4\eta-3)a_s g_0 + \frac{16}{15\pi}(41-33\eta)\eta a_s g_0\right] \quad (6)$$

$$\eta = \frac{1}{2}(1+e) \quad (7)$$

The term φ_{gs} describes the damping of the particles' fluctuating velocities caused by the drag forces between the gas and solid phase. The solids pressure p_s represents the normal force due to particle interactions. The solid-phase stress tensor demands for its calculation the employment of the solid bulk viscosity λ_s, which is the measure of a fluids dissipative resistance to compression, and the solids shear viscosity, which is the summation of dissipative tangential forces due to shearing particle interactions (collisions, kinetic and frictional viscosity). In this work the Syamlal expression for the kinetic solid viscosity was employed. The formulas that correspond to the aforementioned values are as follows [60,63]:

$$\varphi_{gs} = -3K_{gs}\Theta_s \quad (8)$$

$$p_s = \Theta_s\rho_s a_s + 2\rho_s(1+e)a_s^2 g_0\Theta_s \quad (9)$$

$$\overrightarrow{\tau_s} = [\lambda_s\nabla\bullet\overrightarrow{u_s}]\overrightarrow{I} + 2\mu_s\overrightarrow{S_s} \quad (10)$$

$$\overrightarrow{S_s} = \frac{1}{2}\left[(\nabla\overrightarrow{u_s}) + (\nabla\overrightarrow{u_s})^T\right] - \frac{1}{3}\nabla\bullet\overrightarrow{u_s}\overrightarrow{I} \quad (11)$$

$$\lambda_s = \frac{4}{3}a_s\rho_s d_s g_0(1+e)\left(\frac{\Theta}{\pi}\right)^{\frac{1}{2}} \quad (12)$$

$$\mu_s = \mu_{s,coll} + \mu_{s,kin} + \mu_{s,fr} \quad (13)$$

$$\mu_{s,coll} = \frac{4}{5}a_s^2\rho_s d_s g_0(1+e)\left(\frac{\Theta}{\pi}\right)^{\frac{1}{2}} \quad (14)$$

$$\mu_{s,fr} = \frac{p_s\sin(\gamma)}{2\sqrt{I_{2D}}} \quad (15)$$

$$\mu_{s,kin} = \frac{a_s\rho_s d_p\sqrt{\pi\Theta}}{6(3-e)}\left[1 + \frac{2}{5}(1+e)(3e-1)g_0 a_s\right] \quad (16)$$

With regards to the drag function, the Adjusted Syamlal-O'Brien model was employed. Therefore, the following expression was used for the derivation of the interphase exchange coefficient K_{gs} [63]:

$$K_{gs} = \frac{3a_s a_g\rho_g}{4u_{r,s}^2 d_s}C_D\left(\frac{Re_s}{u_{r,s}}\right)|\overrightarrow{u_s} - \overrightarrow{u_g}| \quad (17)$$

where the drag coefficient C_D and the solids terminal velocity $u_{r,s}$ are expressed as:

$$C_D = \left(0.63 + \frac{4.8}{\sqrt{Re_s/u_{r,s}}}\right)^2 \quad (18)$$

$$u_{r,s} = 0.5\left(A - 0.06Re_s + \sqrt{(0.06Re_s)^2 + 0.12Re_s(2B-A) + A^2}\right) \quad (19)$$
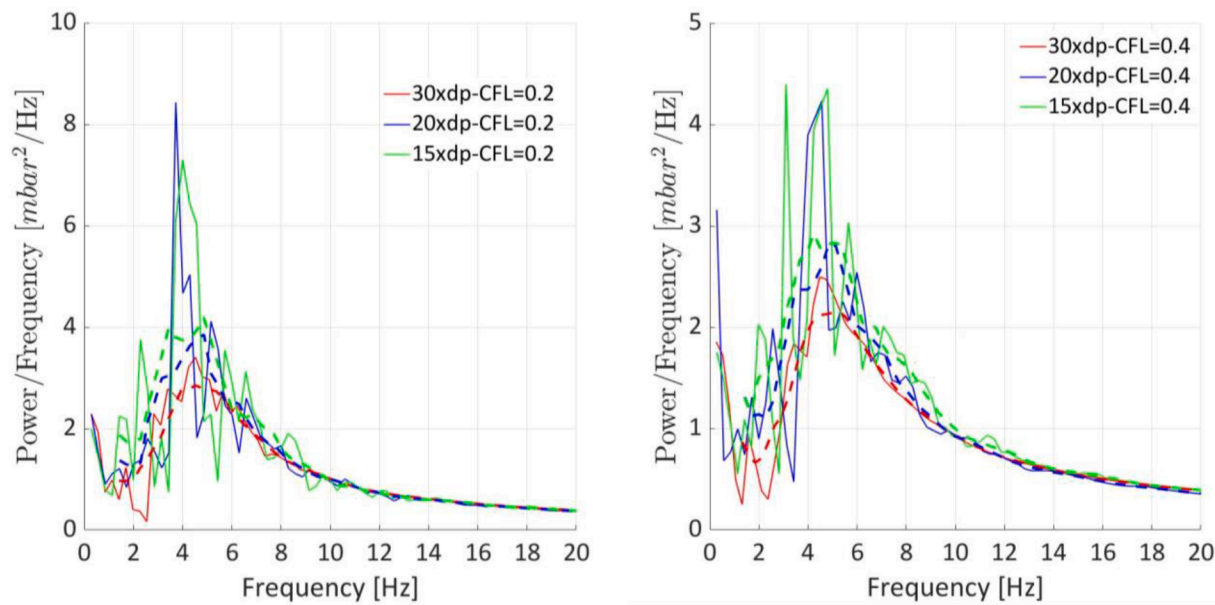
$$A = a_g^{4.14} \quad (20)$$

Fig. 5. Power spectrum of pressure drop over the bed area for the simulations of the IHBFBSR without side-flow for different mesh densities and CFL = 0.2 (left) and CFL = 0.4 (right). With the dotted line, the corresponding Savitzky – Golay filtered spectrum (polynomial order: 1, frame length: 9).

$$B = \begin{cases} 0.8a_g^{1.28} & (a_g \leq 0.85) \\ a_g^{2.65} & (a_g > 0.85) \end{cases} \qquad (21)$$

4. Computational fluid dynamics

Within this work, 3D simulations of the IHBFBSR fluidization behaviour were performed. Simulations were performed in Ansys Fluent 19.2 on a computational cluster (28 cores, 56 threads, 2.40 – 3.30 GHz frequency). With the exception of the biomass feeding inlet, the reactor can be considered as almost axisymmetric, except for the two rings of 25 tuyeres at the bottom of the reactor. This allows for simulation using a periodically repeating "wedge" of either $360/25 = 14.4°$ or $360/5 = 72°$. The $72°$ wedge offers a good compromise between reducing the domain as much as possible and at the same time ensuring that the biomass feeder's side flow does not propagate outside the selected region and influence the hydrodynamics outside the selected domain. Selecting the even smaller wedge would require less computational resources and would have proven to be a much faster option, however would also entail the risk of not properly encapsulating the side-flow's effect on its entirety. It should also be mentioned that the bottom radiant tube burner constituted the "inner wall" of the aforementioned domain, with the actual reactor wall constituting its "outer wall". Therefore, the bottom radiant tube burner is considered in the simulations through the effects of its boundaries on the hydrodynamic behaviour. The assumption that the biomass feeder side-flow's effect does not propagate out of its section will be evaluated from the simulation results. The simulations presented within this work were performed with and without the presence of this side-flow. Another assumption was made with regards to the modelling of the flow entering the reactor through the tuyeres. As mentioned in Section 2, the tuyeres openings are pointed downwards at an angle of $20°$ and their very small diameter leads to an individual inlet velocity which is many orders of magnitude higher (450 m/s) than the dispersed bulk velocity, leading to a time step in the order of 10^{-5} s being required to meet the Courant-Friedrichs-Lewy (CFL) condition. In order to achieve reasonable time steps for the subsequent simulations, the plane corresponding to the top of the tuyeres (height of 33 mm) was assumed to be the bottom of the simulation domain. In this plane the whole cross-sectional area, except for the tops of the tuyeres, was considered to be gas flow inlet. The inlet velocity was assumed to be uniform due to the strong dispersing effect of the granular particles around and below this plane. The total simulation height was 1 m, the width was 97.72 cm and the side-flow inlet was approximated with 16 points. Finally, regarding meshing, polyhedrons were used and all meshes had a maximum aspect ratio of 10. Grid independency tests were performed with 15, 20 and 30 times the bed particle diameter (d_p) grid sizes and are presented in the following section.

An overview of the species property settings is presented in Table A1 in **Appendix A**. The time step was calculated using the approximation presented in **Eq. (22)**:

$$\Delta t \approx \frac{CFL \cdot \Delta z}{u_z} \qquad (22)$$

where Δz was approximated based on the grid density, u_z was assumed to be equal to the bottom inlet velocity and *CFL* values of 0.2 and 0.4 were selected. The effect of the CFL values on the simulations behaviour is discussed in the following section. An overview of the simulation settings employed is presented in Table A2 in **Appendix A**. Within the system, all temperatures for the boundary conditions were assumed to be stable at 600 °C, while a no-slip condition was assumed for the burner walls, the reactor wall and the tuyeres. The inlet was modelled as a velocity inlet and the outlet as a pressure outlet. A symmetry boundary condition was also enforced in the azimuthal direction. For the flux of granular temperature at the wall, the Johnson and Jackson boundary condition was employed [64] as shown in **Eq. (23)**.

$$q_s = \frac{\pi}{6} \sqrt{3} \varphi \frac{a_s}{a_{s,max}} \rho_\sigma g_0 \sqrt{\Theta} u_{wall} - \frac{\pi}{4} \sqrt{3} \frac{a_s}{a_{s,max}} \left(1 - e_{s-wall}^2\right) \rho_s g_0 \Theta^{\frac{3}{2}} \qquad (23)$$

Since the Johnson and Jackson condition is used in combination with the no-slip condition, the specularity coefficient φ becomes equal to 1. The particle – wall restitution coefficient e_{s-wall} was assumed equal to 0.2 for this study. With regards to the particle – particle restitution coefficient, values between 0.8 and 0.99 were examined.

The determination of the bed height from the simulations was performed by locating the maximum in the gradient of the averaged solid volume fraction. The location of this gradient was approximated by employing an adaptation of the methodology described by Mahajan et al. [65]. In particular, the height of the mesh was divided in 1 cm slices and for each slice the average void fraction was calculated. Subsequently, the derivative of the void fraction versus the height was

(a)

(b)

(c)
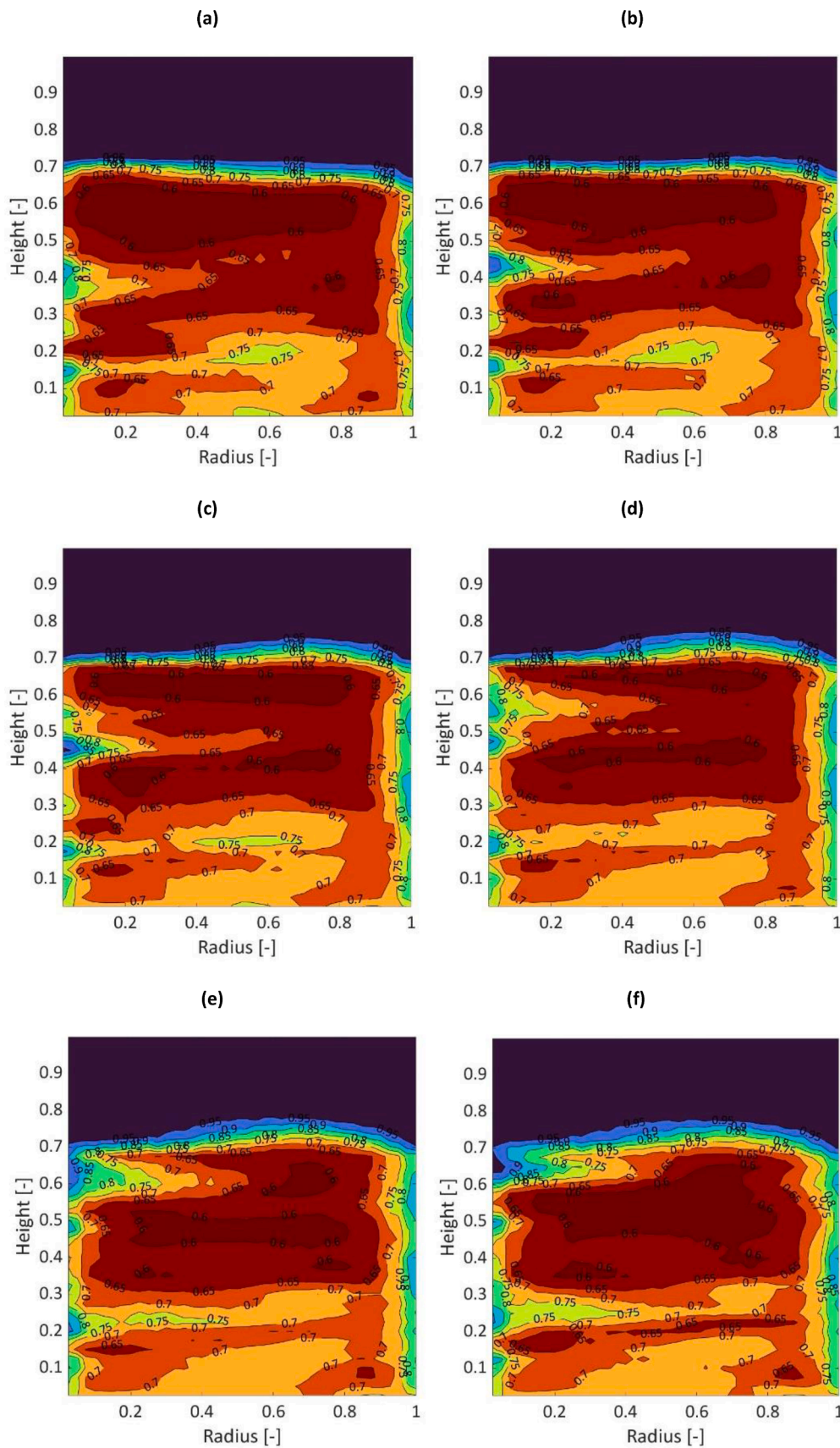
(d)

(e)

(f)

Fig. 6. Instantaneous void fraction contours, showing the movement of bubbles (light orange) that tend to emerge at the inner wall at a dominant frequency of 4 Hz for the $15 \times d_p$ – CFL = 0.2 case. Time starts at 2.25 s at a step of 0.0317 s moving from (a) to (f).

calculated using linear interpolation and finally the bed height was derived as the height corresponding to the maximum gradient.

5. Results

5.1. Mesh and time step independence (without side-flow)

The mesh and time independence of the developed model was examined based on the pressure drop over the bed area and the fluidized bed height. The pressure drop is measured over the reactor volume between the heights of the two pressure gauges P02 and P03, as described in Section 2. The mesh and time step independence tests were performed for combinations of CFL equal to 0.2 and 0.4 and grid sizes 15, 20 and 30 times the bed material particle diameter (d_p). The results of the tests in regards to the pressure drop over the bed area are presented in Fig. 4. The average values obtained from the mesh and time step independence tests are presented in Table B.1 in **Appendix B**.

In Fig. 4, an initial spike in the pressure drop over the bed was observed in all cases, corresponding to the initial bed expansion and the subsequent collapse. After this point, the observed pressure fluctuations can be connected to bubble eruption at the top of the bed and its implosion thereafter. Overall, the magnitude of the fluctuations decreased for coarser meshes, leading to the potential loss of information for meshes larger than $30 \times d_p$. Regarding the effect of CFL variation for a specific mesh size, only a minor effect was apparent in the pressure drop behaviour. In particular, the average difference between the mean pressure drop, calculated between 1 and 3 s, ranged between 0.5 and 1.5 mbar (Table B.1 - **Appendix B**). However, it can also be noted that the magnitude of the fluctuations was slightly smaller for higher CFL values, especially for the case of CFL = 0.4. As mentioned before, for the latter case a loss of information due to the coarser mesh size employed exacerbates the much smaller effect of the time step increase. In general, it can be argued that an increase of CFL leads to minor accuracy losses, significantly lower than the effect of a mesh size increase. Therefore, no firm indication exists that a further decrease of the CFL and therefore the time step, would lead to significantly improved accuracy.

To determine the dominant pressure drop fluctuation frequency for the aforementioned simulations, fast Fourier transform (FFT) analysis was performed. This can provide an insight in the bubble frequency and associated particle mixing in a fluidized bed [65]. The resulting power spectra are presented in Fig. 5, along with the Savitzky – Golay filtered spectra, for noise elimination purposes. The dominant frequency values for the unfiltered spectra obtained from the different mesh density/CFL combination simulations ranged between 3.1 and 4.6 Hz. The observed difference in terms of dominant frequency is small between the various combinations and it can be even smaller qualitatively, if the case of $15 \times d_p$ is considered. Fig. 5 shows that the dominant frequency of 3.1 Hz for the $15 \times d_p$ – CFL = 0.4 case is followed by a peak at ~ 4.6 Hz with a slightly lower magnitude. Overall, the behaviour in terms of bubble formation, as can be derived from the power spectrum of the pressure drop over the bed, was similar for the $20 \times d_p$ and $15 \times d_p$ simulations. For the $30 \times d_p$ cases, despite the qualitative agreement in terms of the location of the dominant frequency, less and broader peaks could be identified. This is indicative of the more gradual eruptions of the bubbles as they break up into the freeboard region, resulting from less sharply defined bubble edges due to the lower mesh density employed. Regarding the effect of CFL on the dominant power frequency, no clear trend could be derived also for this case. The void fraction contours corresponding to the dominant frequency for the $15 \times dp$ – CFL = 0.2 case are presented in Fig. 6. There, the movement of bubbles (light orange) that tend to emerge at the inner wall of the reactor can be clearly observed. In Fig. 6, the $\times$ – axis denotes the dimensionless radius (0 corresponds to the inner-burner wall and 1 to the outer-reactor wall), while the y – axis shows the dimensionless height of the simulated domain, as they were introduced in Section 4.

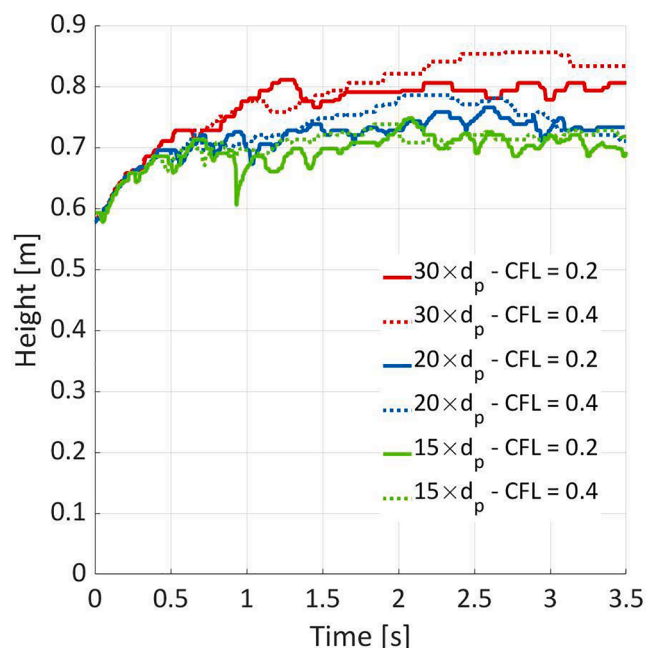The determination of the bed height for the mesh and time step

Fig. 7. Bed height for different mesh density and CFL combinations for the simulations of the IHBFBSR without side-flow.

Table 2
Average pressure drop (dp), dominant frequency (Savitzky-Golay filter) and bed height derived from simulations with different values of the restitution coefficient. The average pressure drop was calculated in the 0.75 – 3.5 s interval and the bed height from 2.5 to 3.5 s, both after stabilization.

Restitution coefficient (-)	Average dp (mbar)	Dominant frequency (Hz)	Bed height (m)
0.8	65.5	5.1	0.72
0.85	64.1	4.8	0.71
0.9	64.4	4.2	0.71
0.95	65.3	4.0	0.73
0.99	66.2	5.1	0.76

independence tests was performed using the method described in Section 4 and the results are presented in Fig. 7. Focusing on the bed height after stabilization, i.e. after 2.5 s of simulation time, it is clear that a decrease of the mesh size from $30 \times d_p$ to $15 \times d_p$, led to a decrease of the bed height. Nevertheless, the difference between the $20 \times d_p$ and $15 \times d_p$ cases was only 0.03 and 0.04 m, for CFL values of 0.2 and 0.4, respectively. The reduction of the time step from CFL = 0.4 to CFL = 0.2, led to a 4.8, 2.6 and 1.4 % reduction of the bed height for the cases of $30 \times d_p$, $20 \times d_p$ and $15 \times d_p$, respectively.

Overall, the bed height derived from all simulations is well within the range deduced from the experimental results (0.67–0.82 m), with the exception of the $30 \times d_p$ – CFL = 0.4 case. Furthermore, the aforementioned bed height reduction for decreasing CFL values becomes less significant for coarser mesh size. In addition, smaller differences were observed between the $20 \times d_p$ and $15 \times d_p$ cases in that regard. When the pressure drop dominant frequency is considered, the $20 \times d_p$ and $15 \times d_p$ cases again presented similar behaviour, in slight contrast with the $30 \times d_p$ case, where the observed peaks were broader. Considering these conclusions from the analysis of the simulations performed, as well as the lack of any useful ones from the pressure drop analysis, the $15 \times d_p$ mesh size was employed in the subsequent simulations. From the analysis performed, it became apparent that the simulation results were more sensitive towards variations of the grid size, rather than the time step size, a conclusion also derived in [66]. Therefore, both CFL values of 0.2 and 0.4 were employed in the following analysis.
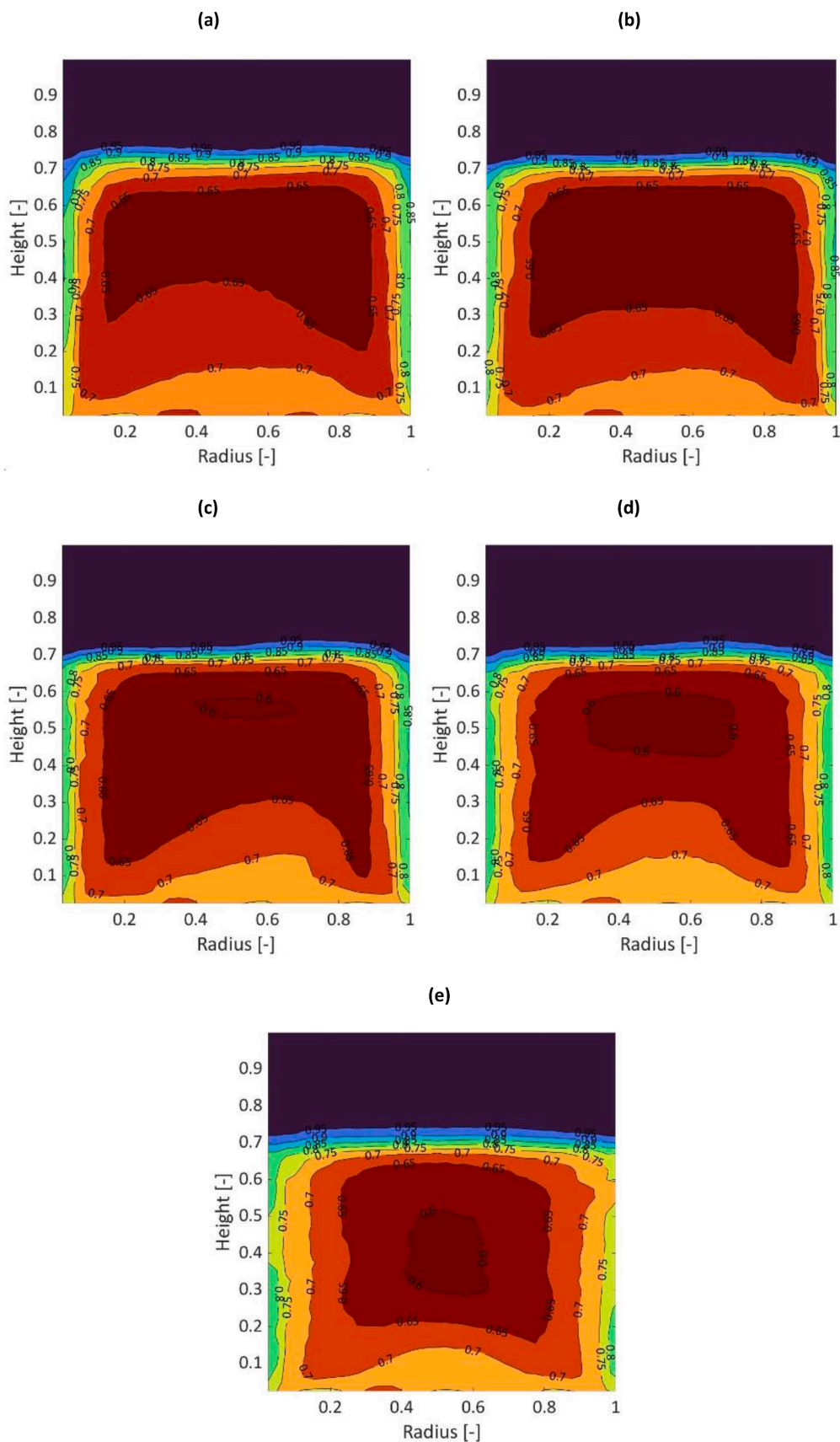
Fig. 8. Time averaged void fraction contours of the IHBFBSR bed area for different values of the restitution coefficient: (a) e = 0.8, (b) e = 0.85, (c) e = 0.9, (d) e = 0.95 and (e) e = 0.99. The simulations were performed with a 15 × d$_p$ grid and a CFL of 0.4.

5.2. Restitution coefficient (without side-flow)

The restitution coefficient determines the degree of exchange of energy and momentum during particle collisions. A restitution coefficient of 1 corresponds to perfectly elastic collisions, while 0 corresponds to inelastic collisions. For sand-like material such as corundum, the typical range of values for the restitution coefficient employed in similar studies is between 0.9 and 0.99 [67–70]. However, in the context of this work, values of restitution coefficient between 0.8 and 0.99 were investigated. It should be mentioned, that a restitution coefficient of 0.9 was employed in the simulations presented in the previous section. The average pressure drop, the dominant frequency and the bed height derived from the restitution coefficient simulations, are presented in Table 2. The simulations were performed with a 15 × d$_p$ grid and a CFL of 0.4.

From Table 2, the minor influence of the restitution coefficient on the main simulation performance metrics employed in this work, can be clearly seen. For the average pressure drop, a standard deviation of 1 % was obtained for the five values investigated, while for the bed height the corresponding value was 3 %. Regarding the bed height, a slight increase was observed for higher values of restitution coefficient of 0.95 and 0.99. In the case of the dominant frequency, due to the presence of

significant amount of noise in the data (especially in the e = 0.85 case), a Savitzky-Golay filter of 1st polynomial order and a frame length of 9 was applied. From this analysis, a 11 % standard deviation between the five values of restitution coefficient was obtained. The dominant frequency values, ranging between 4 and 5.1 Hz, showcased the small influence of restitution coefficient also in this regard. From these findings, it can be derived that the selection of the restitution coefficient value within this range, does not influence the three main metrics considered significantly, as has also been observed in literature [68]. Therefore, a value of 0.9 for the restitution coefficient was selected for the subsequent simulations. However, it remains valuable to examine its effect on the fluidization behaviour of the IHBFBSR. In Fig. 8, the time averaged void fraction contours for all investigated restitution coefficient values are presented.

From Fig. 8, it can be readily derived that the bubbles tend to move towards the inner and outer wall, leaving the highest solids density in the centre of the bed. With decreasing restitution coefficient values, the lowest void fraction area (voidage lower than 0.6), clearly observable at the centre of the bed for 0.99, becomes wider and thinner for values of 0.95 and 0.9, before disappearing completely for 0.85. This could be an indication of improved mixing of the bed for lower values of restitution coefficient, something that has also been reported in the literature [70].
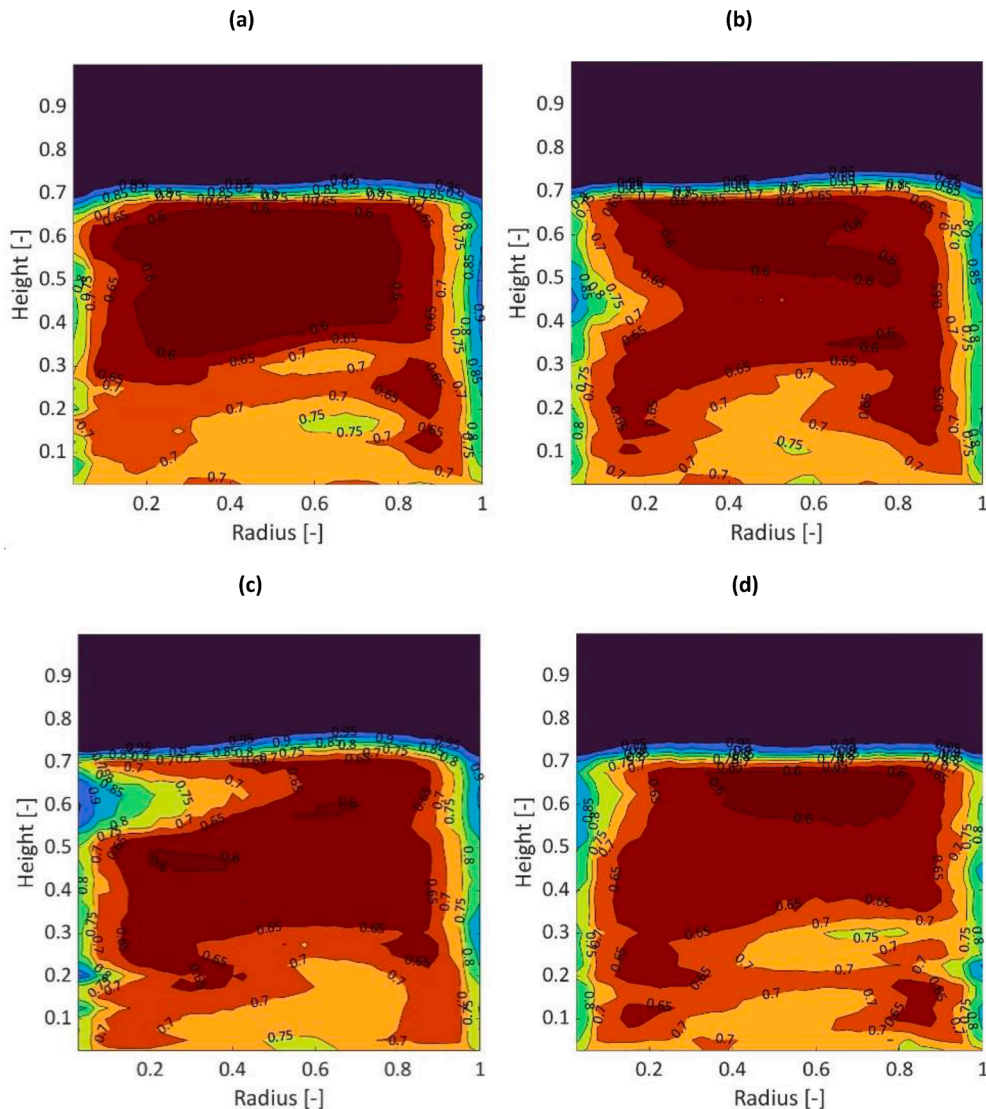

Fig. 9. Void fraction contours of the IHBFBSR bed area at t = 1.26 s (a), t = 1.89 s (b), t = 2.52 s (c), and t = 3.16 s (d). The simulation was performed with a 15 × d$_p$ grid and a CFL of 0.4.

Finally, the void fraction in the area between 0.15 and 0.4 radius and 0.15 – 0.35 height, presents higher void fraction values for restitution coefficient values decreasing from 0.9 to 0.85 to 0.8. Therefore, it can be concluded, that a further reduction of the restitution coefficient enhances the already significant channelling behaviour of the gas flow near the inner wall of the IHBFBSR. Similar behaviour can also be observed at the outer wall, where areas with void fraction above 0.8 start to appear for restitution coefficient values lower than 0.95. These trends suggest that for decreasing values of restitution coefficient, most of the particles tend to cluster towards the top of the bed area forcing the gas to flow along the inner and outer walls.

5.3. IHBFBSR simulation results (without side-flow)

The previous subsection focused on time-averaged voidages. We now aim to get more insight in the bubble behaviour by focusing on the evolution of the instantaneous voidage distribution for a fixed restitution coefficient of e = 0.9 in Fig. 9. The lack of bubble formation in the middle of the reactor becomes readily apparent, since the area between 0.25 and 0.9 radius is dominated by the presence of solid clusters, which become more compact with increasing height. As can be deduced by studying Fig. 9, the few bubbles that are formed in the middle of the reactor, do not seem to be able to penetrate the low void fraction area above them. This conclusion is derived by considering the high void fraction areas, corresponding to bubbles, noted in the general area between 0.5 and 0.8 radius. By piecing together the information provided by the contours in Fig. 9, it can be argued that some bubbles formed in the middle of the reactor, after initially traversing through the bed material particles (a to c), reach a point where they are forced to move towards the side of the reactor (d), unable to pass through the dense top part residing in the middle. Connected to this, the gas flow appears to prefer the pathway along the inner (burner) and outer walls of the reactor. This becomes even more apparent by studying the time averaged void fraction contour in Fig. 8 (c). The presence of the relatively thin high void fraction layers at the sides, indicate that the bubbles are moving up the sides of the reactor, behaving like a slug flow (channelling). This means that a significant amount of particles are trickling down the reactor walls, as large slow-moving bubbles are being formed. Again from Fig. 8 (c), these high void fraction layers seem rather similar in terms of thickness. This, along with the fact that the outer wall area is significantly larger than the inner one, leads to the conclusion that the bubbles at the outer wall of the reactor are larger than the ones near the burner. Furthermore, the lower void fraction zones at the bottom of the reactor, clearly observable in Fig. 9 (a) – (d), are most probably due to the walls corresponding to the tuyeres heads. Finally, note that the low void fraction area at the middle of the reactor appears to tilt towards the right side (outer reactor wall). This could be an indication of a circulating particle flow along the horizontal direction of the reactor, caused by the slug flow along the walls of the reactor (channelling).

The gas volume fraction and velocity vector field at the last time step of the simulation are presented in Fig. 10. The selected time step corresponds to a stabilized state of the bed and therefore can be considered representative of the overall fluidization behaviour of the IHBFBSR. From this figure the previously derived conclusions are verified, since the higher velocities in the system (which correspond to bubbles [19]) as well as the higher void fraction areas, are located mainly in the upper part of the outer and inner walls of the reactor.
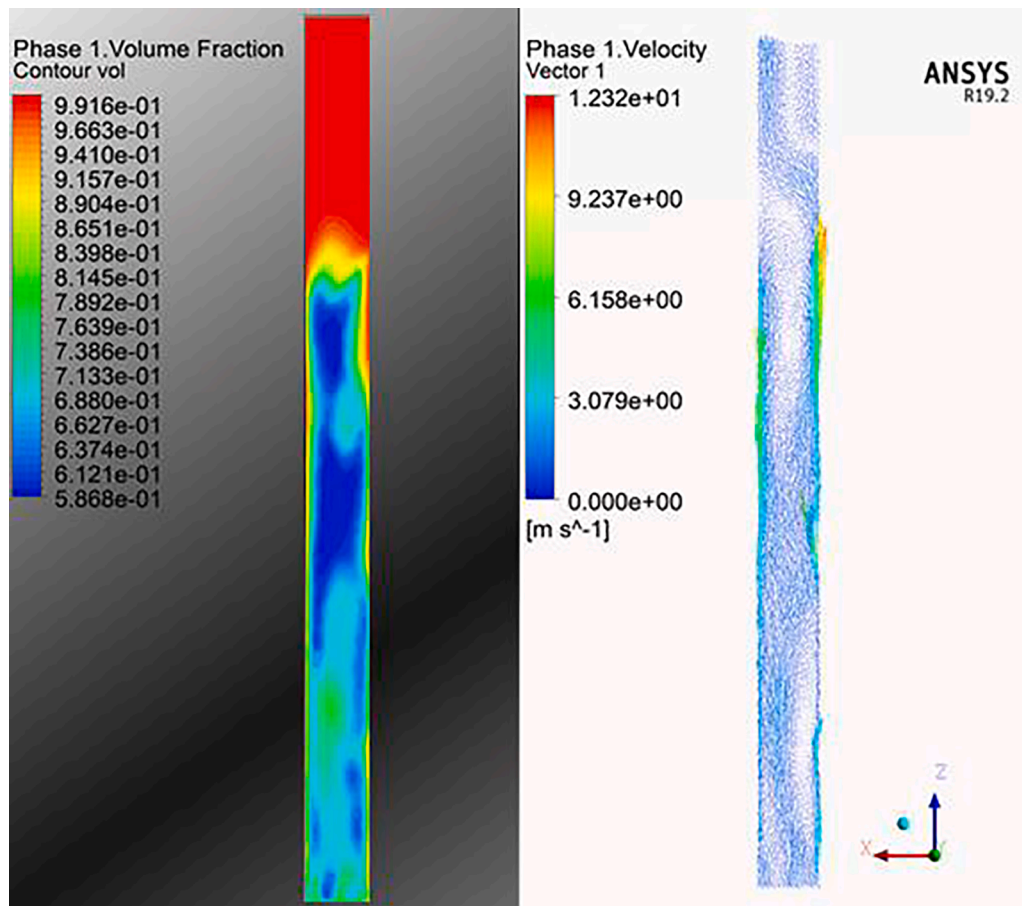

Fig. 10. Gas volume fraction (left) and velocity vector field (right) from the final time step of the IHBFBSR bed area simulation without side-flow. The simulation was performed with a 15 × d_p grid and a CFL of 0.4.

(a)   **(b)**

(c)   **(d)**

(e)   **(f)**

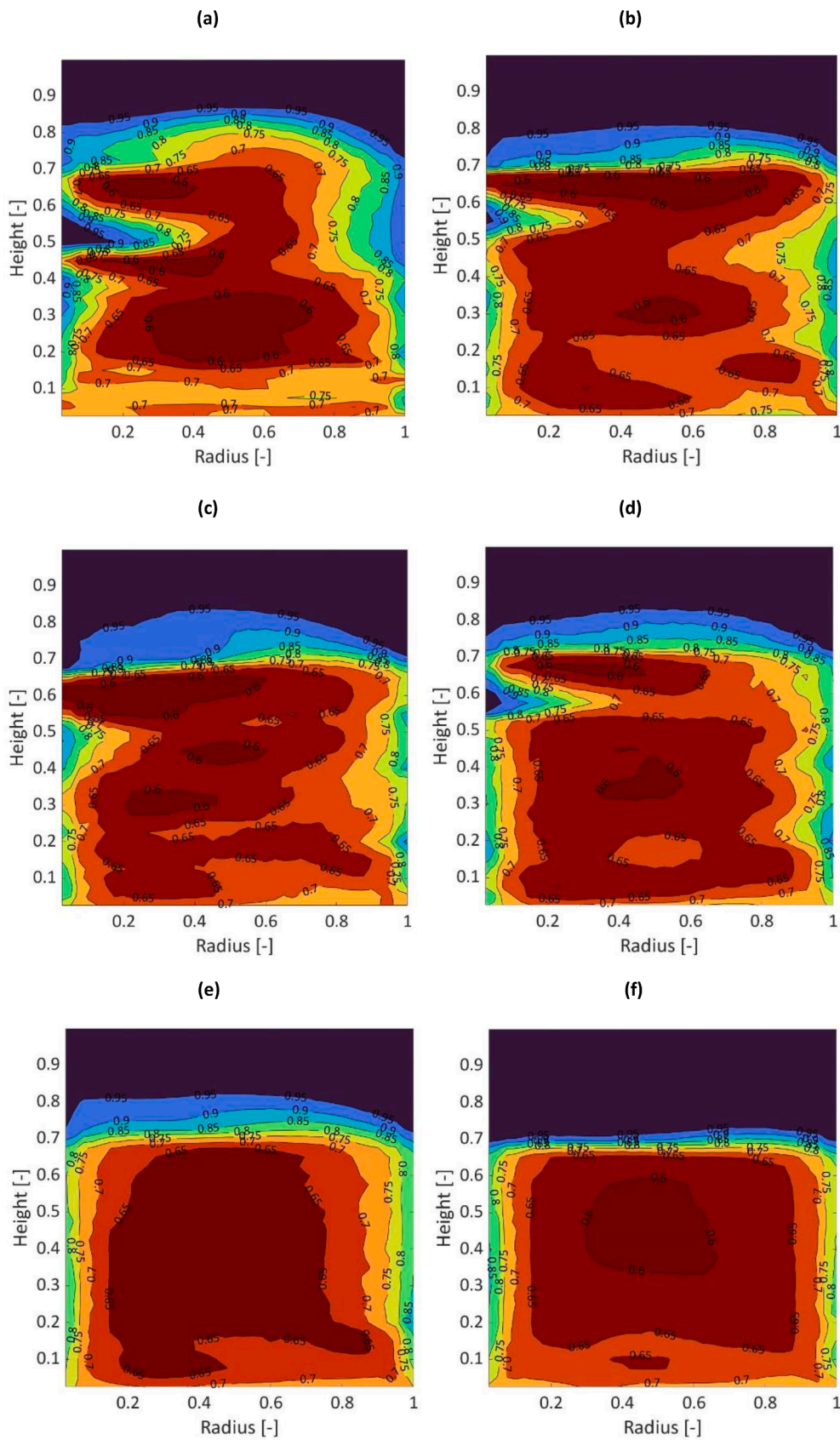**Fig. 11.** Void fraction contours of the IHBFBSR bed area at t = 0.92 s (a), t = 1.84 s (b), t = 2.76 s (c) and t = 3.69 s (d). In (e) and (f) the time averaged void fraction contours for the side-flow and no side-flow cases, respectively. The simulation was performed with a 15 × d$_p$ grid and a CFL of 0.2. The feeder side-flow is located at the outer wall at a dimensionless height of 0.2025.

5.4. Effect of the N_2 purge side-flow on the IHBFBSR fluidization behaviour

In the previous section, the simulation of the fluidization behaviour of the IHBFBSR bed area for a 72° "wedge" was presented. However, as was discussed in Section 2.1 Reactor description, in the experimental system an additional N_2 feed is employed for the pressurization of the feeding system, preventing the back-flow of gases from the main reactor. As a result, a stream of N_2 enters the reactor through the feeder located at the outer wall. The effect of this flow was assumed to be local, within the 72° partition including the feeder outlet. In this section, the testing of this assumption is presented, along with the overall fluidization behaviour including this side-flow. The simulations were performed with a mesh size of 15 × dp, as in the previous cases. Nevertheless, due to the higher gas velocities in the system due to the introduction of the side-flow, the CFL had to be reduced to 0.2. According to the time step independence analysis presented in 5.1, this is not expected to

jeopardize the comparability with the previously conducted simulations with CFL = 0.4. The void fraction contours at four different time-steps of the simulation and the time averaged one are presented in Fig. 11.

As it was also the case for the no side-flow simulations presented in Section 5.3, the formation of bubbles at the inner (burner) wall of the reactor can be clearly observed in Fig. 11 (a) – (d). On the contrary, the formation of bubbles near the outer radius of the reactor is not as apparent as in the previous case. In particular, it appears that the side-flow behaves almost like a stream on the reactor wall, as it passes through the bed area. This particular behaviour also prevents the formation of bubbles near the outer wall of the reactor. This is also noticeable in the comparison of the time averaged void fraction contours of the side-flow and no side-flow simulations presented in Fig. 11 (e) and (f), showing that the inner radius void fraction layers are similar in both cases. Regarding the outer radius, the high void fraction layer (above 0.7) becomes thicker (roughly from 0.85 to 1 radius, versus 0.95 to 1) for the side-flow case. Additionally, sub-layers with void-fraction of 0.8 and
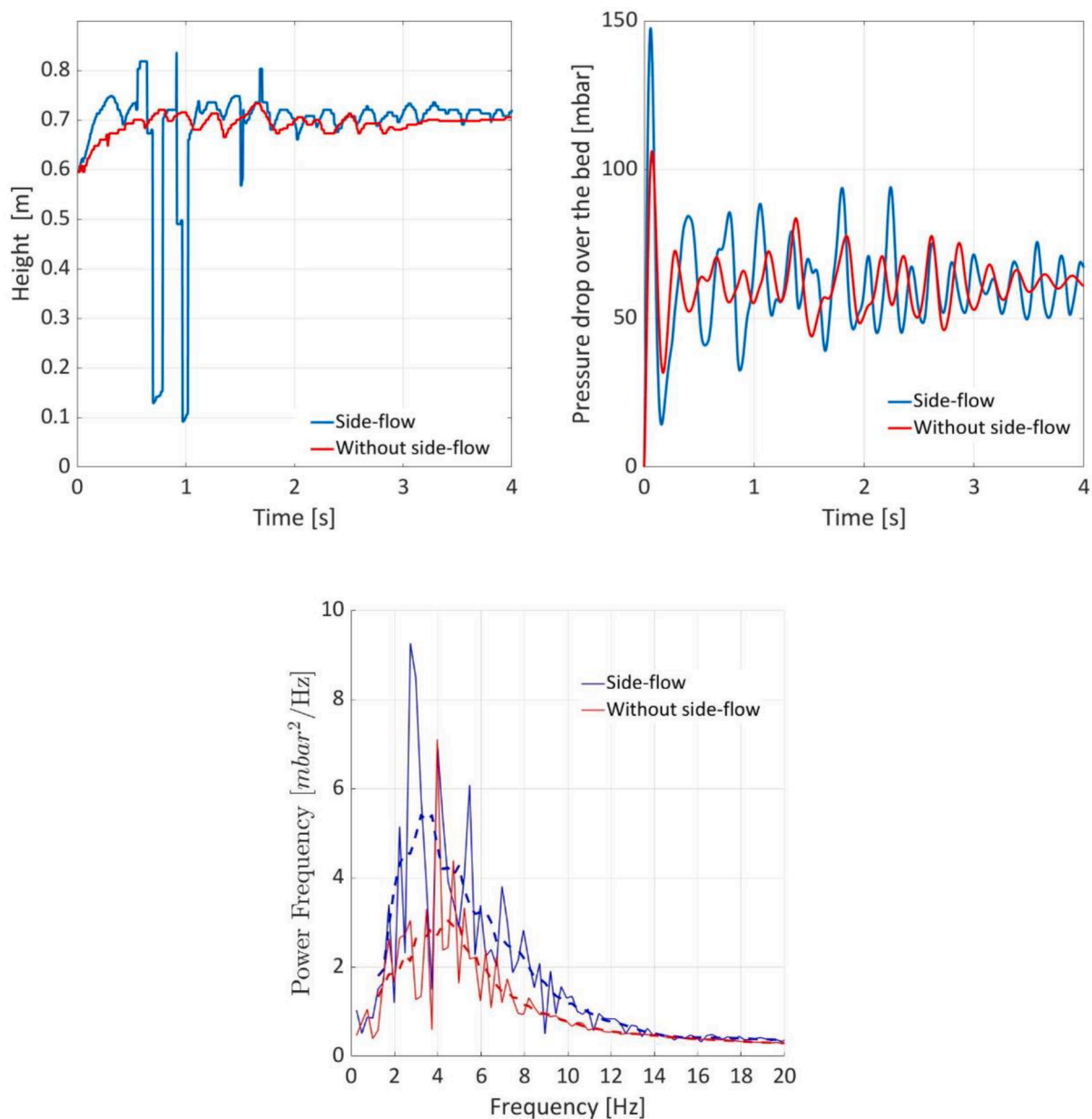
Fig. 12. Comparison of the bed height (left), pressure drop over the bed (right) and power spectrum of pressure drop over the bed area (bottom) from the simulations of the IHBFBSR with (blue) and without (red lines) side-flow. The simulation was performed with a 15 × d_p grid and a CFL of 0.2. In the power spectrum graph (bottom), with the dotted line, the corresponding Savitzky – Golay filtered spectra (polynomial order: 1, frame length: 9).
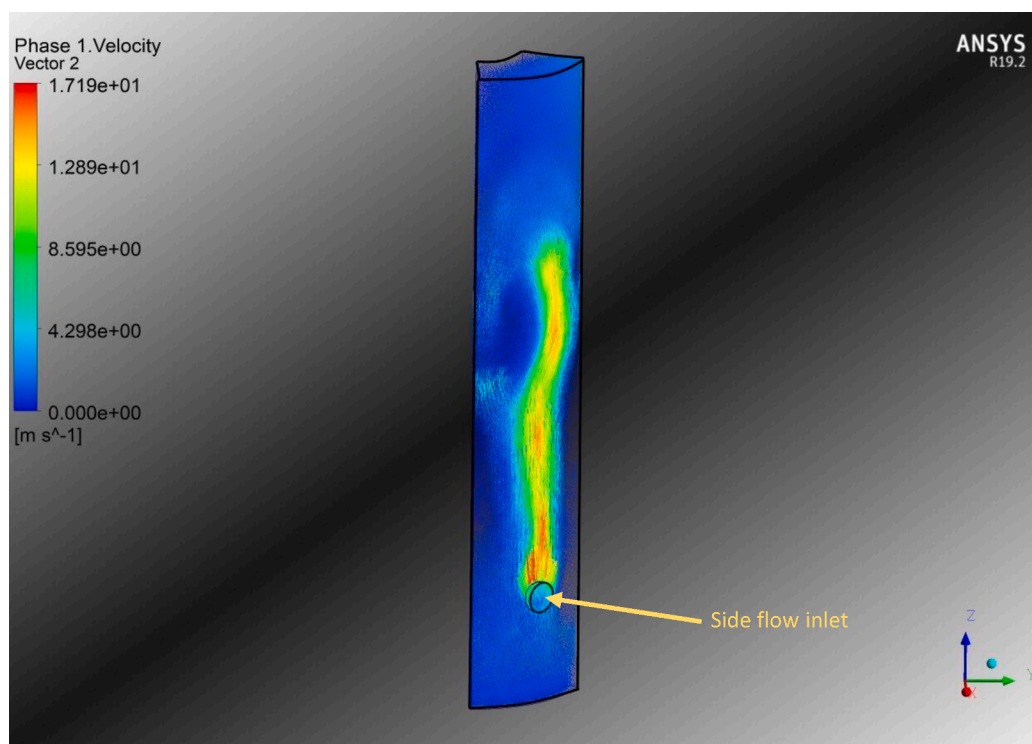
Fig. 13. Velocity vectors of the gas phase from the simulations of the IHBFBSR with side-flow. The simulation was performed with a 15 × dp grid and a CFL of 0.2.

0.85 which were marginally present or not present at all, respectively, for the no side-flow case, are clearly observable in Fig. 11 (e). Another observation can be made in regards to the low void fraction area in the centre of the reactor. As was discussed in the previous section, the central low void fraction area for the case of no side-flow, presented a tilt towards the outer radius of the reactor. This tilt, which is also observable in Fig. 11 (f), is reversed for the case of the side-flow inclusion, due to the aforementioned stream-like flow pattern with which this flow is introduced in the reactor. In particular, it appears that bed particles tend to concentrate more towards the burner wall, hinting towards an increased channelling of the flow towards the outer reactor wall. Another difference between the two cases lies in the presence of low void fraction areas in the centre of the reactor. For the side-flow case, despite the fact that the different void fraction zones present more complex morphologies, mostly 0.6 and 0.65 void fraction zones can be observed. On the other hand, as was discussed for Fig. 9, bubbles appear to form also in the middle of the reactor, although to a much smaller extent. Nevertheless, the lack of void fraction zones lower than 0.65 and the aforementioned complex shapes formed in the centre of the reactor for the side-flow case, can indicate better mixing for this particular case throughout the height of the reactor. It should be reminded, that in the no side-flow case, the 0.25–0.9 radius area was dominated by particle clusters, which became more compact for increasing height.

The method for the determination of the bed height from the simulations performed was described in Section 4. For the simulations with the inclusion of the N₂ purge side-flow, the algorithm had a difficulty in determining the bed height for the first 2 s of the simulations. This phenomenon occurred due to the presence of height layers with a high void fraction. These layers are visible in Fig. 11 approximately from 0.7 to 0.8 height, something that was not the case for the no side-flow simulations. The abovementioned fact, along with the more intense bubble formation at the burner wall of the reactor, can lead the algorithm to identify the void fraction gradient caused by the bubble's presence as the bed height. This phenomenon can be observed in Fig. 12 until roughly 2 s. After this point the behaviour stabilizes and the corresponding bed height is comparable to the case without the side-flow,

albeit a little bit higher (0.72 versus 0.71 m). In regards to the average pressure drop over the bed, the inclusion of the side-flow to the simulations did not lead to a differentiation to its values. This could be attributed to the extreme channelling behaviour as observed in the void fraction contours, since the side-flow passes through the bed without effective obstacles. However, the pressure drop oscillations' magnitude was marginally higher for the case of the side-flow. This can be attributed to the more intense fluidization due to the larger amount of fluidization media and thus higher fluidization velocities employed. Finally, in regards to the dominant frequency, the corresponding values for the unfiltered spectra were 4 and 2.7 Hz for the cases without and with the side-flow, respectively (Fig. 12). The corresponding values for the Savitzky – Golay filtered spectra were similar both in terms of magnitude and difference between the two cases (4.5 and 3.2 Hz, respectively). While it was expected that an increase in the overall fluidization velocity would lead to an increase of the dominant frequency, this was not observed. However, with the increase of the fluidization velocity imposed by the inclusion of the side-flow in the simulations, the number and height of the peaks observed increased. This observation, as it was for the more intense pressure oscillations noted before, is a result of the increased amount of fluidization media in the reactor.

As was mentioned in the beginning of this section, the validity of the reduction of the reactor's geometry to 72° partitions is assured as long as the side-flow does not propagate out of the respective domain. In order to investigate the validity of this assumption, the velocity vectors of the gas phase were computed and subsequently visualised in Fig. 13. Depending on the time step, the flow moves slightly right or left from the feeder inlet, staying always far away enough from the symmetry boundary condition side walls to validate the aforementioned assumption. It can even be argued, that the geometry domain could be further reduced to 36°, although at the loss of the observation of the waving effect in the radial direction of the side-flow stream. Such a decrease of the geometry's size would improve the computational requirements, allowing further decrease of the time step or mesh size.

Overall, our results show that the side-flow is not well mixed in the

reactor. Therefore there is a possibility that in practice a cold spot is formed at the feeder inlet. The presence of such as a cold spot, would render the assumption that the N_2 side-flow is at the same temperature as the rest of the reactor at this point (600 °C) incorrect. In this case, the volume expansion of the N_2 gas caused by the temperature increase would also affect the internal flow field in ways not covered by the present simulations. Furthermore, as was also shown by Ostermeier et al. [71], the gas inlet geometry does not influence the global properties of bed height and pressure drop greatly. However, our work shows that it has a big influence on the gas and particle flow fields and solids distribution. The implementation of heat and mass transfer modelling in future simulations by the authors will allow the more in-depth investigation of this particular effect. Finally, regarding the bed height (0.72 with side-flow and 0.71 without side-flow) derived from the simulations, it was always within the limits imposed by the experiments (0.67 – 0.82 m). However, given the fact that for setting up of the Syamlal model, a minimum fluidization velocity including the side-flow was employed, the overall height computed might be over-predicted. Considering the behaviour of the side-flow presented in this work, it might be more appropriate to exclude it from the calculation of the minimum fluidization velocity of the corundum bed, since its effect appears to be insignificant. This conclusion is also supported by the clear over-prediction that can be observed for the pressure drop over the bed area. In particular, the experimentally derived average pressure drop of 55 mbar is over-predicted by 12.5 % in the side-flow simulations.

6. Conclusions

In this work, CFD – TFM simulations of a novel 50 kW$_{th}$ indirectly heated bubbling fluidized bed steam reformer (IHBFBSR) were performed to investigate its hydrodynamic behaviour. The results were verified with the employment of corresponding experimental results obtained from fluidization experiments conducted in a pilot-scale reactor. The hydrodynamic behaviour of the reactor was simulated successfully, as evident by the small deviations observed between the experimental and computational values obtained for the global hydrodynamic metrics (bed height and pressure drop). It was shown that for realistic values of the particle restitution coefficient channelling of the gas flow occurs near the reactor walls. This channelling was present for both the side-flow and no side-flow simulations. However, larger bubbles appeared to be forming near the outer wall of the reactor for the no side-flow simulations, while the opposite behaviour was encountered for the side-flow simulations. This was due to the stream-like behaviour of the side-flow moving against the outer wall of the reactor, thus preventing the formation of bubbles locally. Additionally, limiting the simulations to a 72° symmetry "wedge" was validated by the model findings, which indicated that even further reduction is possible. Overall, it can be argued that an increase of the reactor's diameter could potentially lead to a reduction of the observed channelling of the fluidization media and improve the mixing achieved in the reactor. This could in turn improve the heat and mass transfer in the system and thus also increase the conversion efficiency of the IHBFBSR during gasification experiments.

Overall, the present work constitutes the first step in an effort to study the fluidization behaviour of the novel IHBFBSR reactor of TU Delft. This investigation of this geometrically unique fluidized bed hydrodynamics lays the groundwork for future heat and mass transfer, as well as chemical reaction modelling which will allow the introduction and exploration of more experimental variables in conjunction with the simulation work. Apart from further verifying the simulation work performed so far, such an approach will allow the utilization of the entire spectrum of the IHBFBSR's analytical/instrumentation capabilities, something that was practically impossible within the context of the present work.

Declaration of Competing Interest

The authors declare that they have no known competing financial interests or personal relationships that could have appeared to influence the work reported in this paper.

Appendix A

.

Table A1
Ansys Fluent species property settings.

Parameter	Input
Air	
Phase type	Eulerian
Density	Ideal Gas Law
Viscosity	Kinetic Theory
Molecular Weight (kg/kmol)	28.966
Corundum	
Phase type	Granular
Density	3950
Bulk density (kg/m^3)	1636
Particle diameter	543 μm
Granular temperature model	PDE
Granular viscosity	Syamlal O'Brien
Granular bulk viscosity	Lun et. al [61] (kg/ms)
Granular conductivity	Syamlal O'Brien
Solids pressure	Lun et. al [61]
Elasticity modulus	Derived
Packing limit (-)	0.4141
Wall	
Fluent database	Default settings
Roughness constant (-)	0.5
Granular condition	Johnson – Jackson
Wall restitution coefficient (-)	0.2

Table A2
Ansys Fluent simulations settings.

Parameter	Input
Model	TFM
Volume fraction parameter formulation	Implicit
Simulation dimension	3D
Drag model	Adjusted Syamlal
Restitution coefficient	0.8 – 0.99
Convergence continuity	10^{-4}
Convergence (remaining)	Default
Turbulence model settings	
K – epsilon model	Realizable
Near – wall treatment	Standard wall functions
Turbulence multiphase model	Mixture
Model constants	Default
Run conditions	
Grid size	Variable
Time steps	Variable
Max iterations	2000 – 3000
Data frequency	Variable

Appendix B

.

Table B1
Pressure drop over the bed (dp) (mean, maximum and minimum) and dominant frequency values calculated between 1 and 3 s of the simulation and bed height (from 2.5 to 3.5 s) for the mesh density/CFL combinations used in the independence tests without side-flow.

Mesh size	CFL	Mean dp (mbar)	Max dp (mbar)	Min dp (mbar)	Dominant frequency (Hz)	Bed height (m)
$30 \times d_p$	0.2	67.3	72.7	61.7	4.5	0.79
$30 \times d_p$	0.4	67.8	71.0	63.3	4.5	0.83
$20 \times d_p$	0.2	66.1	85.2	45.3	3.7	0.74
$20 \times d_p$	0.4	64.6	73.3	57.8	4.6	0.76
$15 \times d_p$	0.2	64.4	86.9	49.2	4.0	0.71
$15 \times d_p$	0.4	65.0	76.1	51.3	3.1	0.72
Experimental		55.0	60.7	46.7	n.a.	0.67–0.82

References

[1] S. Wang, G. Dai, H. Yang, Z. Luo, Lignocellulosic biomass pyrolysis mechanism: A state-of-the-art review, Prog. Energy Combust. Sci. 62 (2017) 33–86.
[2] P. Basu, Biomass gasification and pyrolysis practical design and theory, Elsevier Inc., 2010.
[3] V.S. Sikarwar, M. Zhao, P. Clough, J. Yao, X. Zhong, M.Z. Memon, N. Shah, E. J. Anthony, P.S. Fennell, An overview of advances in biomass gasification, Energy Environ. Sci. 9 (10) (2016) 2939–2977.
[4] V. Belgiorno, G. De Feo, C. Della Rocca, R.M.A. Napoli, Energy from gasification of solid wastes, Waste Manage. 23 (1) (2003) 1–15.
[5] A. Gómez-Barea, M. Suárez-Almeida, A. Ghoniem, Analysis of fluidized bed gasification of biomass assisted by solar-heated particles, Biomass Convers. Biorefin. 11 (1) (2021) 143–158.
[6] O. Levenspiel, What will come after petroleum? Ind. Eng. Chem. Res. 44 (2005) 5073–5078.
[7] J. Karl, T. Pröll, Steam gasification of biomass in dual fluidized bed gasifiers: A review, Renew. Sustain. Energy Rev. 98 (2018) 64–78.
[8] J.C. Schmid, F. Benedikt, J. Fuchs, A.M. Mauerhofer, S. Müller, H. Hofbauer, Syngas for biorefineries from thermochemical gasification of lignocellulosic fuels and residues—5 years' experience with an advanced dual fluidized bed gasifier design, Biomass Convers. Biorefin. 11 (6) (2021) 2405–2442.
[9] K. Fürsatz, J. Fuchs, F. Benedikt, M. Kuba, H. Hofbauer, Effect of biomass fuel ash and bed material on the product gas composition in DFB steam gasification, Energy 219 (2021) 119650.
[10] A. Larsson, M. Kuba, T. Berdugo Vilches, M. Seemann, H. Hofbauer, H. Thunman, Steam gasification of biomass – Typical gas quality and operational strategies derived from industrial-scale plants, Fuel Process. Technol. 212 (2021), 106609.
[11] N. Hanchate, S. Ramani, C.S. Mathpati, V.H. Dalvi, Biomass gasification using dual fluidized bed gasification systems: A review, J. Cleaner Prod. 280 (2021) 123148.
[12] H. Jüntgen, K.H. Van Heek, Gasification of coal with steam using heat from HTRs, Nucl. Eng. Des. 34 (1) (1975) 59–63.
[13] J. Karl, Biomass heat pipe reformer—design and performance of an indirectly heated steam gasifier, Biomass Convers. Biorefin. 4 (1) (2014) 1–14.
[14] R.H. Williams, E.D. Larson, R.E. Katofsky, J. Chen, Methanol and hydrogen from biomass for transportation, Energy for Sustainable Development 1 (5) (1995) 18–34.
[15] G. Gallmetzer, P. Ackermann, A. Schweiger, T. Kienberger, T. Gröbl, H. Walter, M. Zankl, M. Kröner, The Agnion Heatpipe-Reformer—operating experiences and evaluation of fuel conversion and syngas composition, Biomass Convers. Biorefin. 2 (3) (2012) 207–215.
[16] J.M. Leimert, P. Treiber, J. Karl, The Heatpipe Reformer with optimized combustor design for enhanced cold gas efficiency, Fuel Process. Technol. 141 (2016) 68–73.
[17] S. Karellas, J. Karl, E. Kakaras, An innovative biomass gasification process and its coupling with microturbine and fuel cell systems, Energy 33 (2008) 284–291.
[18] V. Verma, J.T. Padding, N.G. Deen, J.A.M. Kuipers, Numerical Investigation on the Effect of Pressure on Fluidization in a 3D Fluidized Bed, Ind. Eng. Chem. Res. 53 (2014) 17487–17498.
[19] D. Kunii, O. Levenspiel, Fluidization Engineering, 2nd ed., Butterworth-Heinemann, 1991.
[20] M.A. van der Hoef, M. Ye, M. van Sint Annaland, A.T. Andrews, S. Sundaresan, J.A. M. Kuipers, Multiscale Modeling of Gas-Fluidized Beds, in: G.B. Marin (Ed.), Advances in Chemical Engineering, Academic Press, 2006, pp. 65–149.

[21] K. Qiu, F. Wu, S. Yang, K. Luo, K.K. Luo, J. Fan, Heat transfer and erosion mechanisms of an immersed tube in a bubbling fluidized bed: A LES–DEM approach, Int. J. Therm. Sci. 100 (2016) 357–371.
[22] H. Wahyudi, K. Chu, A. Yu, 3D particle-scale modeling of gas–solids flow and heat transfer in fluidized beds with an immersed tube, Int. J. Heat Mass Transf. 97 (2016) 521–537.
[23] Y. Zhao, M. Jiang, Y. Liu, J. Zheng, Particle-scale simulation of the flow and heat transfer behaviors in fluidized bed with immersed tube, AIChE J. 55 (2009) 3109–3124.
[24] H. Ma, Y. Zhao, Y. Cheng, CFD-DEM modeling of rod-like particles in a fluidized bed with complex geometry, Powder Technol. 344 (2019) 673–683.
[25] S. Yang, K. Luo, J. Fan, K. Cen, Particle-Scale Investigation of the Hydrodynamics and Tube Erosion Property in a Three-Dimensional (3-D) Bubbling Fluidized Bed with Immersed Tubes, Ind. Eng. Chem. Res. 53 (2014) 6896–6912.
[26] L. Zhou, Y. Zhao, CFD-DEM simulation of fluidized bed with an immersed tube using a coarse-grain model, Chem. Eng. Sci. 231 (2021), 116290.
[27] JiXu PengZhao, XingchiLiu, WeiGe, JunwuWang, A computational fluid dynamics-discrete element-immersed boundary method for Cartesian grid simulation of heat transfer in compressible gas–solid flow with complex geometries, Phys. Fluids 32 (2020), 103306.
[28] P. Zhao, J. Xu, W. Ge, J. Wang, A CFD-DEM-IBM method for Cartesian grid simulation of gas-solid flow in complex geometries, Chem. Eng. J. 389 (2020), 124343.
[29] Y. Guo, C.-Y. Wu, C. Thornton, Modeling gas-particle two-phase flows with complex and moving boundaries using DEM-CFD with an immersed boundary method, AIChE J. 59 (2013) 1075–1087.
[30] M. Chen, Z. Chen, H. Gong, Y. Tang, M. Liu, CFD–DEM–VDGM method for simulation of particle fluidization behavior in multi-ring inclined-hole spouted fluidized bed, Particuology 57 (2021) 112–126.
[31] J. Su, Z. Gu, X.Y. Xu, Discrete element simulation of particle flow in arbitrarily complex geometries, Chem. Eng. Sci. 66 (2011) 6069–6088.
[32] J.-F. Dietiker, T. Li, R. Garg, M. Shahnam, Cartesian grid simulations of gas–solids flow systems with complex geometry, Powder Technol. 235 (2013) 696–705.
[33] T. Li, J.-F. Dietiker, Y. Zhang, M. Shahnam, Cartesian grid simulations of bubbling fluidized beds with a horizontal tube bundle, Chem. Eng. Sci. 66 (2011) 6220–6231.
[34] K. Cheng, Y. Wang, Q. Yang, A semi-resolved CFD-DEM model for seepage-induced fine particle migration in gap-graded soils, Comput. Geotech. 100 (2018) 30–51.
[35] Q. Yang, K. Cheng, Y. Wang, M. Ahmad, Improvement of semi-resolved CFD-DEM model for seepage-induced fine-particle migration: Eliminate limitation on mesh refinement, Comput. Geotech. 110 (2019) 1–18.
[36] N. Gui, J.R. Fan, K. Luo, DEM–LES study of 3-D bubbling fluidized bed with immersed tubes, Chem. Eng. Sci. 63 (2008) 3654–3663.
[37] N. Gui, J. Fan, Numerical simulation of pulsed fluidized bed with immersed tubes using DEM–LES coupling method, Chem. Eng. Sci. 64 (2009) 2590–2598.
[38] Y. Mori, C.-Y. Wu, M. Sakai, Validation study on a scaling law model of the DEM in industrial gas-solid flows, Powder Technol. 343 (2019) 101–112.
[39] C.L. Wu, A.S. Berrouk, K. Nandakumar, Three-dimensional discrete particle model for gas–solid fluidized beds on unstructured mesh, Chem. Eng. J. 152 (2009) 514–529.
[40] C.L. Wu, J.M. Zhan, Y.S. Li, K.S. Lam, Dense particulate flow model on unstructured mesh, Chem. Eng. Sci. 61 (2006) 5726–5741.
[41] J.I. Córcoles, A. Acosta-Iborra, J.A. Almendros-Ibáñez, Influence of immersed surface shape on the heat transfer process and flow pattern in a fluidized bed using numerical simulation, Int. J. Heat Mass Transf. 178 (2021), 121621.
[42] M. Fattahi, S.H. Hosseini, G. Ahmadi, A. Parvareh, Numerical simulation of heat transfer coefficient around different immersed bodies in a fluidized bed containing Geldart B particles, Int. J. Heat Mass Transf. 141 (2019) 353–366.
[43] Z. Hau, E.W.C. Lim, Heat Transfer from an Immersed Tube in a Bubbling Fluidized Bed, Ind. Eng. Chem. Res. 55 (2016) 9040–9053.
[44] S.I. Ngo, Y.-I. Lim, D. Lee, M.W. Seo, Flow behavior and heat transfer in bubbling fluidized-bed with immersed heat exchange tubes for CO2 methanation, Powder Technol. 380 (2021) 462–474.
[45] E.M.L. Sin, E.W.C. Lim, Heat transfer from immersed tubes in a pulsating fluidized bed, Powder Technol. 327 (2018) 500–511.
[46] Y. He, W. Zhan, Y. Zhao, H. Lu, I. Schlaberg, Prediction on immersed tubes erosion using two-fluid model in a bubbling fluidized bed, Chem. Eng. Sci. 64 (2009) 3072–3082.
[47] N.H. Dong, L.M. Armstrong, S. Gu, K.H. Luo, Effect of tube shape on the hydrodynamics and tube-to-bed heat transfer in fluidized beds, Appl. Therm. Eng. 60 (2013) 472–479.
[48] L.M. Armstrong, S. Gu, K.H. Luo, The influence of multiple tubes on the tube-to-bed heat transfer in a fluidised bed, Int. J. Multiph. Flow 36 (2010) 916–929.
[49] H. Vogtenhuber, D. Pernsteiner, R. Hofmann, Experimental and Numerical Investigations on Heat Transfer of Bare Tubes in a Bubbling Fluidized Bed with Respect to Better Heat Integration in Temperature Swing Adsorption Systems, Energies 12 (2019) 2646.
[50] M. Schreiber, T.W. Asegehegn, H.J. Krautz, Numerical and Experimental Investigation of Bubbling Gas-Solid Fluidized Beds with Dense Immersed Tube Bundles, Ind. Eng. Chem. Res. 50 (2011) 7653–7666.
[51] S. Jaso, H. Arellano-Garcia, G. Wozny, Oxidative coupling of methane in a fluidized bed reactor: Influence of feeding policy, hydrodynamics, and reactor geometry, Chem. Eng. J. 171 (2011) 255–271.
[52] J.F. de Jong, M. van Sint Annaland, J.A.M. Kuipers, Membrane-assisted fluidized beds—Part 2: Numerical study on the hydrodynamics around immersed gas-permeating membrane tubes, Chem. Eng. Sci. 84 (2012) 822–833.

[53] V. Verma, T. Li, J.-F. Dietiker, W.A. Rogers, Hydrodynamics of gas–solids flow in a bubbling fluidized bed with immersed vertical U-tube banks, Chem. Eng. J. 287 (2016) 727–743.

[54] C. Tsekos, M. del Grosso, W. de Jong, Gasification of woody biomass in a novel indirectly heated bubbling fluidized bed steam reformer, Fuel Process. Technol. 224 (2021), 107003.

[55] M.H. Uddin, C.J. Coronella, Effects of grid size on predictions of bed expansion in bubbling fluidized beds of Geldart B particles: A generalized rule for a grid-independent solution of TFM simulations, Particuology 34 (2017) 61–69.

[56] M. Adnan, J. Sun, N. Ahmad, J.J. Wei, Multiscale modeling of bubbling fluidized bed reactors using a hybrid Eulerian-Lagrangian dense discrete phase approach, Powder Technol. 376 (2020) 296–319.

[57] O. Levenspiel, Chemical Reaction Engineering, 3d ed., John Wiley & Sons, 1998.

[58] M. Siedlecki, PhD Thesis: On the gasification of biomass in a steam-oxygen blown CFB gasifier with the focus on gas quality upgrading: technology background, experiments and mathematical modeling, in, Delft University of Technology, 2011.

[59] J. Ding, D. Gidaspow, A bubbling fluidization model using kinetic theory of granular flow, AIChE J. 36 (1990) 523–538.

[60] D. Gidaspow, Multiphase Flow and Fluidization: Continuum and Kinetic Theory Descriptions, Academic Press, New York, 1994.

[61] C.K.K. Lun, S.B. Savage, D.J. Jeffrey, N. Chepurniy, Kinetic theories for granular flow: inelastic particles in Couette flow and slightly inelastic particles in a general flowfield, J. Fluid Mech. 140 (1984) 223–256.

[62] S. Ogawa, A. Umemura, N. Oshima, On the equations of fully fluidized granular materials, Zeitschrift für angewandte Mathematik und Physik, ZAMP 31 (1980) 483–493.

[63] M. Syamlal, T.J. O'Brien, Computer simulation of bubbles in a fluidized bed, A.I. Ch.E, Symposium Series 85 (1989) 22–31.

[64] P.C. Johnson, R. Jackson, Frictional–collisional constitutive relations for granular materials, with application to plane shearing, J. Fluid Mech. 176 (1987) 67–93.

[65] V.V. Mahajan, J.T. Padding, T.M.J. Nijssen, K.A. Buist, J.A.M. Kuipers, Nonspherical particles in a pseudo-2D fluidized bed: Experimental study, AIChE J. 64 (5) (2018) 1573–1590.

[66] P. Ostermeier, S. DeYoung, A. Vandersickel, S. Gleis, H. Spliethoff, Comprehensive investigation and comparison of TFM, DenseDPM and CFD-DEM for dense fluidized beds, Chem. Eng. Sci. 196 (2019) 291–309.

[67] J. Wang, M.A. van der Hoef, J.A.M. Kuipers, Comparison of Two-Fluid and Discrete Particle Modeling of Dense Gas-Particle Flows in Gas-Fluidized Beds, Chem. Ing. Tech. 85 (2013) 290–298.

[68] M. Adnan, J. Sun, N. Ahmad, J.J. Wei, Comparative CFD modeling of a bubbling bed using a Eulerian-Eulerian two-fluid model (TFM) and a Eulerian-Lagrangian dense discrete phase model (DDPM), Powder Technol. 383 (2021) 418–442.

[69] N. Almohammed, F. Alobaid, M. Breuer, B. Epple, A comparative study on the influence of the gas flow rate on the hydrodynamics of a gas–solid spouted fluidized bed using Euler-Euler and Euler–Lagrange/DEM models, Powder Technol. 264 (2014) 343–364.

[70] T. Wang, T. Tang, Q. Gao, Z. Yuan, Y. He, Experimental and numerical investigations on the particle behaviours in a bubbling fluidized bed with binary solids, Powder Technol. 362 (2020) 436–449.

[71] P. Ostermeier, A. Vandersickel, S. Gleis, H. Spliethoff, Three dimensional multi fluid modeling of Geldart B bubbling fluidized bed with complex inlet geometries, Powder Technol. 312 (2017) 89–102.